ATLAS CONF Note

ATLAS-CONF-2021-036

26th July 2021

Combination and summary of ATLAS dark matter searches using 139 fb^{-1} of $\sqrt{s} = 13$ TeV pp collision data and interpreted in a two-Higgs-doublet model with a pseudoscalar mediator

The ATLAS Collaboration

A combination of two searches for dark matter is presented, along with results from a wide range of experimental analyses that are interpreted in a common benchmark model: a Two-Higgs-Doublet Model with a pseudoscalar mediator. The analyses use up to 139 fb^{-1} of proton–proton collision data at a centre-of-mass energy $\sqrt{s} = 13$ TeV recorded with the ATLAS detector at the LHC between 2015–2018. The results from two searches targetting the $E_{\mathrm{T}}^{\mathrm{miss}} + Z(\ell^{+}\ell^{-})$ and $E_{\mathrm{T}}^{\mathrm{miss}} + h(b\bar{b})$ signatures are combined statistically. The constraints of a wide range of additional experimental analyses, targetting final states with and without invisible particles, are evaluated and summarised alongside the combination in several interpretations within this model.

1 Introduction

The particle nature of dark matter (DM) is one of the major unsolved questions in modern particle physics. There is strong evidence for the existence of a non-luminous form of matter accounting for 85% of the matter content in the universe from astrophysical measurements, including the rotational speed of stars in galaxies, precision measurements of the cosmic microwave background [1, 2], and gravitational lensing measurements [3–5]. The Standard Model of Particle Physics (SM), however, does not contain a particle whose properties are consistent with those observations.

Searches for DM are being conducted at experiments around the world with complementary experimental approaches: indirect searches aim to detect DM in the universe via the observation of its annihilation or decay to SM particles; direct searches are designed to observe the elastic scattering of DM by nuclei and electrons in a detector; finally, searches at particle colliders target the production of DM from high-energy collisions of SM particles.

The ATLAS experiment [6] at the Large Hadron Collider (LHC) [7] is a general-purpose detector that allows for a wide range of DM searches. In the following, the focus will be entirely on the hypothesis that DM is a weakly interacting massive particle (WIMP) [8] and, more specifically, a Dirac fermion. WIMPs could in principle interact with the SM sector in different ways. A particular strength of collider searches lies in the fact that the high-energy collisions of SM particles could not only produce DM directly under controlled experimental conditions but also provide access to particles mediating the interactions between DM and the SM sector. A *mediator* produced in a collision could decay to DM particles, which themselves could not be detected and would lead to missing transverse momentum (with magnitude $E_{\mathrm{T}}^{\mathrm{miss}}$). Alternatively, a mediator could decay back into SM particles, from which its properties could be reconstructed.

Dark matter searches at the LHC explore both avenues in the quest to solve the puzzle of DM. Invisible mediator decays can be detected only if the mediator is produced in association with another particle, for example from initial-state radiation that results in a hadronic jet, leading to a characteristic $E_{\mathrm{T}}^{\mathrm{miss}}$+jet signature [9, 10]. Visible mediator decays allow for the reconstruction of the mediator particle from its decay products, for example in the context of resonance searches, if the mediator is produced in the s-channel [11–15].

The above-mentioned searches are traditionally interpreted in the context of so-called *simplified models* of DM, which rely on a minimal set of new particles and interactions. The most commonly used among these simplified models postulate the existence of a single fermionic DM particle and a single mediator, which, depending on the model, could be a vector, axial-vector, scalar, or pseudo-scalar particle [16–18]. The models are characterised by a minimal set of free parameters, namely the masses of the DM and mediator particles and the couplings of the mediator to the SM and dark sectors.

In this note, a more complete benchmark model is used. It provides an ultra-violet complete and renormalisable framework for the interpretation of DM searches. It is built upon the assumption that the SM Higgs boson is part of an extended Higgs sector with two complex Higgs doublets. This is a key assumption in many theories extending the SM, such as supersymmetry [19]. The interaction between the SM sector and DM in this model is mediated by a pseudoscalar particle a. Pseudoscalar mediators are not strongly constrained by direct-detection experiments because the tree-level amplitude for the DM-nucleon elastic scattering is suppressed by the momentum transfer in the non-relativistic limit [20]. This renders collider searches for these processes particularly useful.

The model, referred to as Two Higgs Doublet Model (2HDM) + pseudoscalar mediator (a), 2HDM+a, is the simplest and currently only gauge-invariant and UV-complete extension of the simplified model with a pseudoscalar mediator, and has been first introduced in Ref. [21]. The model is adopted as a common LHC benchmark model by the LHC Dark Matter Working Group [22], which is a joint forum of theory groups and the ATLAS, CMS, and LHCb collaborations. This model, unlike the simplified models described above, predicts a wide variety of detector signatures. Among the most prominent signatures in the parameter space explored in this note are the production of DM in association with a Higgs boson ($E_{\mathrm{T}}^{\mathrm{miss}}$+$h$ signatures) or with a Z boson ($E_{\mathrm{T}}^{\mathrm{miss}}$+$Z$ signatures). Further signatures are related to DM production in association with a top quark and a W boson ($E_{\mathrm{T}}^{\mathrm{miss}}$+$Wt$), visible decays of the additional heavy Higgs bosons, and invisible decays of the SM Higgs boson to DM.

A summary paper including constraints on the 2HDM+a benchmark based on a variety of dark matter searches using 36 fb^{-1} data of $\sqrt{s}$ = 13 TeV proton-proton collisions has been previously published by the ATLAS Collaboration [23]. Constraints on the model have also been derived by the CMS Collaboration using the results from searches in the $E_{\mathrm{T}}^{\mathrm{miss}} + h(b\bar{b})$ [24] and $E_{\mathrm{T}}^{\mathrm{miss}} + Z(\ell^+\ell^-)$ [25] final states using the 137 fb^{-1}of LHC Run 2 data collected with the CMS detector.

This note updates and extends the constraints on the 2HDM+a compared to Ref. [23] based on a newer and improved set of individual searches using 139 fb^{-1} of data. These searches are sensitive to a range of new phenomena, including but not limited to processes involving DM. This note focuses exclusively on the interpretation of their results in the context of the 2HDM+a benchmark. Apart from the larger dataset, this note contains a number of improvements to enhance the sensitivity across a larger model parameter space. First, results from additional searches and a statistical combination are included in the 2HDM+a re-interpretation to extend the parameter space coverage:

- A statistical combination of two of the most sensitive searches, $E_{\mathrm{T}}^{\mathrm{miss}} + h(b\bar{b})$ [26] and $E_{\mathrm{T}}^{\mathrm{miss}} + Z(\ell^+\ell^-)$ [27]
- The inclusion of two searches not considered in Ref. [23]: a search targeting the $E_{\mathrm{T}}^{\mathrm{miss}} + Wt$ signature [28], and a re-interpretation of a search for charged Higgs bosons decaying to tb [29].

Second, four additional benchmark parameter scans are included to highlight the complementarity of the different searches and extend the model coverage. Finally, $b\bar{b}$-initiated production is now included in the 2HDM+a model interpretations for the $E_{\mathrm{T}}^{\mathrm{miss}}$+$h$ and $E_{\mathrm{T}}^{\mathrm{miss}}$+$Z$ signatures, in addition to the gluon-gluon (gg) initiated production considered in the previous publication. This process is relevant at higher values of $\tan\beta$, the ratio of the two vacuum expectation values (VEVs) of the two Higgs doublets.

This note is organised as follows: The benchmark model and the different parameter scans are introduced in Section 2. The model implementation is described in Section 3. Section 4 provides short explanations of individual DM searches. The statistical combination is described in Section 5. The results of the benchmark scans are shown in Section 6.

2 Model overview

The benchmark model in this note is built upon the assumption of the existence of a second complex Higgs doublet, which is postulated in various ultra-violet-complete (UV-complete) theories with an extended Higgs sector. The 2HDM sector is assumed to have a CP-conserving potential and a softly broken $\mathbb{Z}_2$ symmetry [30]. After electroweak symmetry breaking, the 2HDM contains five Higgs bosons: a lighter CP even boson, h, a heavier CP-even boson, H, a CP-odd boson, A, and two charged bosons, $H^{\pm}$. The 2HDM coupling structure is chosen to be of type-II [30] and the alignment and decoupling limit is assumed, so that the lighter CP-even state h can be identified with the SM Higgs boson.

The 2HDM+a benchmark further postulates the existence of a fermionic DM particle χ and a pseudoscalar (CP-odd) mediator a with Yukawa-like couplings to both the SM fermions and the Dirac DM particle χ, thus allowing for interactions between DM and the SM sector. The mediator couples to SM fermions proportionally to the Higgs Yukawa couplings and mixes with the pseudoscalar A of the 2HDM sector with mixing angle θ.

The phenomenology of the model is fully determined by 14 independent parameters: the masses of the Higgs bosons h, H, A, and $H^{\pm}$; the mass of the mediator a; the mass of the DM particle χ; the Yukawa coupling strength between the mediator and the DM particle, g_{χ}; the electroweak VEV, v; the ratio of the VEVs of the two Higgs doublets, $\tan\beta$; the mixing angles of the CP-even and CP-odd weak eigenstates, α and θ, respectively; and the three quartic couplings between the scalar doublets and the mediator ($\lambda_{P1}, \lambda_{P2}, \lambda_3$).

The values of some of these parameters are heavily constrained by both electroweak and flavour measurements as well as phenomenological considerations, such as the requirement that the Higgs potential is stable. Further parameter choices are driven by the desire to simplify the phenomenology of the model and reduce the space of independent parameters to be scanned by experimental searches. A summary of the parameter choices and the benchmark scans shown in this note is given in the following. A detailed description of the 2HDM+a benchmark scans recommended by the LHC Dark Matter Working Group is given in Ref. [22].

The following parameter settings are common to all benchmark scans shown in Section 6. The coupling g_{χ} is set to unity with a negligible effect on the shapes of the kinematic distributions of interest. As mentioned above, the alignment limit ($\cos(\beta - \alpha) = 0$) is assumed, and hence $m_h = 125$ GeV and $v = 246$ GeV. The quartic coupling $\lambda_3 = 3$ is chosen to ensure the stability of the Higgs potential for our choice of the masses of the heavy Higgs bosons which are themselves fixed to the same value ($m_A = m_H = m_{H^{\pm}}$) to simplify the phenomenology and evade the constraints from electroweak precision measurements [21]. The other quartic couplings are also set to 3 in order to maximise the trilinear couplings between the CP-odd and the CP-even neutral states.

After these considerations, five free parameters remain: the heavy Higgs mass $m_A = m_H = m_{H^{\pm}}$; the pseudoscalar mediator mass m_a; the DM mass m_{χ}; the mixing angle $\sin\theta$ between the two CP-odd states a and A; and VEV ratio $\tan\beta$.

The constraints on the model are evalulated with regard to a number of representative benchmark scans, in which one or two of the free parameters are varied while the others are kept at fixed values:

- **Scan 1**: two 2D scans in (m_a, m_A) assuming $\tan\beta = 1.0$ and
  a. $\sin\theta = 0.35$
  b. $\sin\theta = 0.7$.
- **Scan 2**: two 2D scans in ($m_A, \tan\beta$) assuming $m_a = 250$ GeV and
  a. $\sin\theta = 0.35$
  b. $\sin\theta = 0.7$.

- **Scan 3**: two 2D scans in $(m_a, \tan\beta\,)$ assuming $m_A = 0.6$ TeV and
  a. $\sin\theta = 0.35$
  b. $\sin\theta = 0.7$.
- **Scan 4**: two 1D scans in $\sin\theta$ with $\tan\beta\; = 1.0$ and
  a. $m_A = 0.6$ TeV, $m_a = 200$ GeV (low-mass scan)
  b. $m_A = 1$ TeV, $m_a = 350$ GeV (high-mass scan)
- **Scan 5**: a 1D scan in m_χ assuming $m_A = 0.6$ TeV, $m_a = 250$ GeV, $\tan\beta\; = 1.0$ and $\sin\theta = 0.35$.

Five parameter scans, namely scans 1a, 3a, 4a, 4b, and 5 are recommended by the LHC Dark Matter Working Group [22], and have been used in previous ATLAS publications, most notably Ref. [23]. The additional scans, 1b, 2, and 3b, are motivated by the studies in Refs. [22, 31] and are shown for the first time in this note to further highlight the rich phenomenology of the model. In particular, the choice of $\sin\theta = 0.7 \approx 1/\sqrt{2}$ $(\theta = \pi/4)$ corresponds to maximal mixing in the pseudoscalar sector and is particularly interesting, for example, for the newly introduced $E_{\mathrm{T}}^{\mathrm{miss}} + Wt$ search [31].

In all scans other than the DM mass scan, $m_\chi = 10$ GeV is chosen. The choice of m_χ has a negligible impact on the $E_{\mathrm{T}}^{\mathrm{miss}}$+X signatures for $m_a > 2 \cdot m_\chi$. The chosen value ensures a sizeable branching ratio for the decay $a \to \chi\bar{\chi}$ for all values of $m_a > 100$ GeV that are considered in this note.

Another improvement introduced in this note concerns the production modes of the various Higgs bosons and the pseudoscalar mediator. In Ref. [23], only gg-initiated production was considered. The dominant production modes involving gluon initial states for all four $E_{\mathrm{T}}^{\mathrm{miss}} + X$ signatures discussed in Section 4 are summarised in Figure 1.

In this note, $b\bar{b}$-initiated production is also included, which is particularly relevant for the $E_{\mathrm{T}}^{\mathrm{miss}}$+$Z$ and $E_{\mathrm{T}}^{\mathrm{miss}}$+$h$ signatures at large values of $\tan\beta$, as shown in Section 6. The leading Feynman diagrams for $b\bar{b}$-initiated production of these two signatures are shown in Figure 2.

3 Data and simulated samples

All analyses discussed in this note all rely on data from proton-proton collisions at a centre-of-mass energy of $\sqrt{s} = 13$ TeV collected by the ATLAS detector at the LHC in the years 2015–2018. The integrated luminosity of the dataset, after requiring that all detector subsystems were operational and recording good quality data [32], amounts to 139 fb^{-1}.

Simulated data is used to model the predictions of the 2HDM+a benchmark described in Section 2. This model has been implemented in the Universal FeynRules Output (UFO) format [33]. All signal processes are modelled at leading-order (LO) in the strong coupling constant.

Events were generated from this UFO implementation using the MadGraph5_aMC@NLO [34] Monte Carlo (MC) generator interfaced with Pythia 8 [35] for the modelling of the parton shower and hadronisation with the parameter values set according to the ATLAS tune A14 [36]. The NNPDF3.0NLO set of parton distribution functions (PDF) at next-to-leading order in the five-flavour scheme is used, which assumes a massless b-quark and $\alpha_s(m_Z) = 0.118$ [37]. For consistency, the five-flavour scheme and $m_b = 0$ GeV are chosen for the matrix element (ME) computation in MadGraph5_aMC@NLO for the $b\bar{b}$-initiated

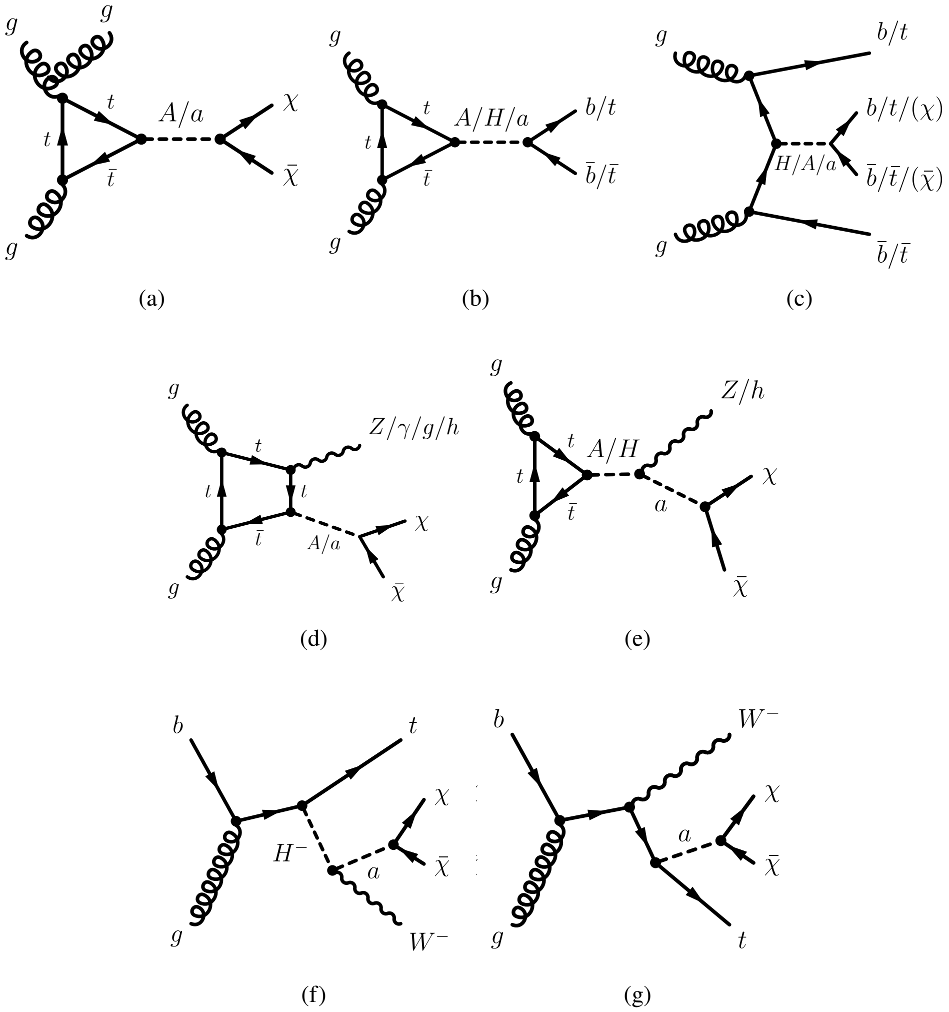

Figure 1: Representative Feynman diagrams for the dominant gluon-induced production and decay modes in the 2HDM+a.

production. For the gg-initiated production the four-flavour scheme is used to include top and bottom quark contributions in the production loop. These modelling choices follow the recommendations of the LHC Dark Matter Working Group [38].

To simulate the effects of additional pp collisions in the same and nearby bunch crossings, additional interactions were generated using the soft QCD processes of PYTHIA 8.186 with the A3 tune [39] and the MSTW2008LO PDF [40], and overlaid onto each simulated hard-scatter event. The simulated samples were reweighted to the pileup distribution observed in data. Simulated events were processed either through a detector simulation [41] based on GEANT4 [42] or through a fast simulation [43] with a parameterisation of the calorimeter response and GEANT4 for the other parts of the detector. All simulated samples were reconstructed in the same manner as the data. Corrections derived from data control samples were applied to simulated events to account for differences between data and simulation in the reconstruction efficiencies, momentum scale and resolution of leptons, and in the efficiency and false positive rate for identifying b-jets.

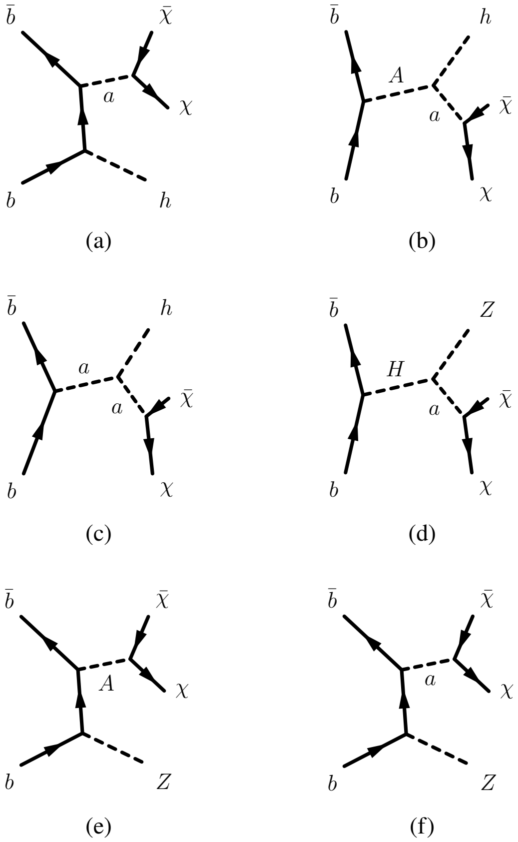

Figure 2: Representative Feynman diagrams for the $b\bar{b}$-initiated production of the $E_{\mathrm{T}}^{\mathrm{miss}} + h$ and $E_{\mathrm{T}}^{\mathrm{miss}} + Z$ signatures in the 2HDM+a.

To produce signal events efficiently across the large multidimensional parameter space of the 2HDM+a, the MadGraph reweighting module [44] was used to obtain predictions for a range of different signal model parameters from a minimal set of actually generated events. This is achieved by assigning new event weights based on the ratios of matrix-elements for the input (generated) and target parameter points. The event weights are calculated on-the-fly during the event generation. This method is validated by comparing weighted distributions with generated ones for a few representative samples. The reweighting yields an immense reduction of the required computing resources as the detector simulation has to be run only once.

4 Individual searches

The results from the following analyses are used to derive constraints on the 2HDM+a parameter space:

1. A search for a leptonically decaying Z boson produced in association with missing energy ($E_{\mathrm{T}}^{\mathrm{miss}} + Z(\ell^+\ell^-)$) [27].
2. Searches for Higgs bosons produced in association with missing energy with the Higgs boson decaying to bottoms quarks ($E_{\mathrm{T}}^{\mathrm{miss}} + h(b\bar{b})$) [26] or photons ($E_{\mathrm{T}}^{\mathrm{miss}} + h(\gamma\gamma)$) [45].

3. A search for DM produced in association with a top quark and a W boson ($E_{\mathrm{T}}^{\mathrm{miss}} + Wt$) [28].
4. A search for charged Higgs bosons $H^{\pm}$ produced in association with a top quark and a bottom quark and decaying to a top and a bottom quark ($H^{\pm}tb$) [29].
5. A preliminary combination of searches for invisible decays of the SM Higgs boson [46].

A brief overview of the analyses is given in the following. The $E_{\mathrm{T}}^{\mathrm{miss}} + Z(\ell^+\ell^-)$ and $E_{\mathrm{T}}^{\mathrm{miss}} + h(b\bar{b})$ searches enter the statistical combination described in Section 5.

4.1 $E_{\mathrm{T}}^{\mathrm{miss}} + Z(\ell^+\ell^-)$

This analysis is designed to search for two leptons ℓ ($\ell = e, \mu$) to form a Z-boson candidate, in association with large $E_{\mathrm{T}}^{\mathrm{miss}}$ [27]. Those leptons are used to trigger the events. The search is optimised for models such as associated production of the Higgs boson (ZH) with the Higgs boson decaying to invisible particles, a simplified DM model with an axial-vector or a vector mediator and the 2HDM+a.

The dominant backgrounds consist of ZZ, WZ, WW, Z+jets and $t\bar{t}$. The events with more than two leptons are rejected to reduce WZ background. Selection requirements on $E_{\mathrm{T}}^{\mathrm{miss}}$ and the $E_{\mathrm{T}}^{\mathrm{miss}}$ significance are applied to suppress the Z+jets background. For the reduction of the WW, $t\bar{t}$ and Z+jets backgrounds, the angle between the two leptons is required to be small. Also, events with a b-jet are not accepted to reduce the $t\bar{t}$ background. Control regions are defined for the dominant background processes as follows: an $e\mu$ control region ($t\bar{t}$- and WW- enriched), a three-lepton control region (WZ-enriched), and a four-lepton control region (ZZ-enriched). Smaller backgrounds are estimated using simulated data. A simultaneous fit of the signal region and control regions is performed for the statistical interpretation. In order to maximise the sensitivity in the wide range of the 2HDM+a parameter space, a transverse mass is used as a discriminant. The transverse mass is calculated from the transverse momentum of the two lepton system and the $E_{\mathrm{T}}^{\mathrm{miss}}$, assuming it is a ZZ system.

No significant deviation from the SM expectations is observed. The results are used to place constraints on a variety of signal processes, including those predicted by the 2HDM+a. These results are included in the combination and summary plots of this note.

The $E_{\mathrm{T}}^{\mathrm{miss}} + Z(\ell^+\ell^-)$ signature has played a minor role in the simplified models with vector mediators [23], compared to the $E_{\mathrm{T}}^{\mathrm{miss}}$+jet signature. In the 2HDM+a parameter spaces explored in this note, however, the $E_{\mathrm{T}}^{\mathrm{miss}} + Z(\ell^+\ell^-)$ signature has dominant contributions as shown in Section 6, while the sensitivity from the $E_{\mathrm{T}}^{\mathrm{miss}}$+jet has been shown to be negligible [22].

4.2 $E_{\mathrm{T}}^{\mathrm{miss}} + h(b\bar{b})$

This analysis uses final states with b-jets and $E_{\mathrm{T}}^{\mathrm{miss}}$ [26]. $E_{\mathrm{T}}^{\mathrm{miss}}$ triggers are used to collect events and a Higgs boson is reconstructed from the b-jet(s). Two signal regions are defined based on the boost of the Higgs boson in the transverse plane. Since the transverse momentum of the Higgs boson is highly correlated with $E_{\mathrm{T}}^{\mathrm{miss}}$, the two regions are separated by $E_{\mathrm{T}}^{\mathrm{miss}}$: $E_{\mathrm{T}}^{\mathrm{miss}} < 500$ GeV and $E_{\mathrm{T}}^{\mathrm{miss}} > 500$ GeV. At low $E_{\mathrm{T}}^{\mathrm{miss}}$ the two b-jets from the Higgs boson decay are well separated and can be reconstructed as two small-radius jets (resolved signal region). As the $E_{\mathrm{T}}^{\mathrm{miss}}$ increases, the two b-jets begin to merge in a single large-radius jet (merged signal region). All signal regions are further split into subregions with exactly two

b-jets or ≥ 3 b-jets. This splitting is meant to enhance the sensitivity to $b\bar{b}$ initiated production, where the Higgs boson and DM particle are produced with an extra pair of b-quarks from gluon splitting (Figure 2).

The dominant backgrounds consist of $t\bar{t}$ and W/Z bosons produced in association with heavy-flavour (HF) jets. The Z+HF becomes dominant as the $E_{\mathrm{T}}^{\mathrm{miss}}$ increases. The events with electrons, muons or taus are rejected to reduce backgrounds. The $t\bar{t}$, W+HF and Z+HF contributions are modelled using simulations with their normalisations corrected from data by using background-enriched control regions requiring one or two charged leptons. A simultaneous fit of signal regions and control regions is performed to obtain limits in 2HDM+a parameter space.

No significant deviation from the SM expectations is observed. The results are used to constrain two common DM benchmark models, including the 2HDM+a. Reference [26] only includes results for the benchmark scan 1a ($m_a - m_A$ plane at $\sin\theta = 0.35$). Constraints on the remaining benchmark scans in Section 2 have been specifically derived for this note using the same procedure as for the results already included in Ref. [26].

Along with $E_{\mathrm{T}}^{\mathrm{miss}} + Z(\ell^+\ell^-)$ channel, this analysis also plays a major role to constrain the 2HDM+a model. Also, the $E_{\mathrm{T}}^{\mathrm{miss}} + h(b\bar{b})$ analysis is complementary to $E_{\mathrm{T}}^{\mathrm{miss}} + Z(\ell^+\ell^-)$ in the benchmark scans described in Section 2 as shown in Section 6.

4.3 $E_{\mathrm{T}}^{\mathrm{miss}} + h(\gamma\gamma)$

The $E_{\mathrm{T}}^{\mathrm{miss}} + h(\gamma\gamma)$ analysis targets final states with two photons and a significant amount of $E_{\mathrm{T}}^{\mathrm{miss}}$ [45]. Events are required to have at least two photon candidates. Two photons with highest energy in the transverse plane are selected to form a Higgs candidate. Those photons are used to trigger the event.

After the photon requirements, events are required to pass a preselection of $E_{\mathrm{T}}^{\mathrm{miss}} > 90$ GeV and $\Delta E_{\mathrm{T}}^{\mathrm{miss}} < 30$ GeV, where $\Delta E_{\mathrm{T}}^{\mathrm{miss}}$ is the $E_{\mathrm{T}}^{\mathrm{miss}}$ calculated from the vertex selected by a neural network minus the $E_{\mathrm{T}}^{\mathrm{miss}}$ calculated from the hardest vertex [45]. Following this preselection, a boosted decision tree (BDT) is trained to discriminate between DM signals and the non-resonant diphoton background, using variables such as $p_{\mathrm{T}}^{\gamma\gamma}$ and the $E_{\mathrm{T}}^{\mathrm{miss}}$ significance as input variables.

Finally, events are separated into low $E_{\mathrm{T}}^{\mathrm{miss}}$ ($E_{\mathrm{T}}^{\mathrm{miss}} < 150$ GeV) and high $E_{\mathrm{T}}^{\mathrm{miss}}$ ($E_{\mathrm{T}}^{\mathrm{miss}} > 150$ GeV) regions. In each region, two categories are defined from two sequential ranges of the BDT score, with the ranges optimised to maximise the combined signal sensitivity in the two chosen categories while discarding the remaining events.

The dominant backgrounds are SM $h \to \gamma\gamma$, non-resonant $\gamma\gamma$, γ+jet, $V\gamma$, and $V\gamma\gamma$. They are extracted by fitting analytic functions to the diphoton invariant mass distribution in the range $105 < m_{\gamma\gamma} < 160$ GeV.

No significant excess above the expected SM background is observed in any of the signal regions. Exclusion limits are thus placed on a selection of DM benchmark models. The exclusion results of Ref. [45] already include the benchmark scans 1a, 2a and 3a. Constraints on the remaining benchmark scans in Section 2 have been derived specifically for this note.

4.4 $E_{\mathrm{T}}^{\mathrm{miss}} + Wt$

This search has been designed specifically to target the production of DM in association with a top quark and a W boson in the context of the 2HDM+a [28]. Unlike the $E_{\mathrm{T}}^{\mathrm{miss}}$+$X$ searches described above, this search is sensitive to diagrams involving charged Higgs boson production, such as the one in Figure 1(f). The on-shell production of the charged Higgs boson in association with a top quark dominates the production cross section for the $E_{\mathrm{T}}^{\mathrm{miss}} + Wt$ signature, if the decay channel $H^{\pm} \rightarrow Wa$ is kinematically accessible.

Several final states are considered, either including one or two leptons (electrons or muons) and a significant amount of $E_{\mathrm{T}}^{\mathrm{miss}}$. The $\mathrm{tW}_{1\mathrm{L}}$ analysis channel targets $Wt + \chi\bar{\chi}$ events where only one of the W bosons decays leptonically, while the $\mathrm{tW}_{2\mathrm{L}}$ analysis channel targets the same signal processes with both W bosons decaying leptonically. The two selections are designed to be mutually exclusive. The results of these two analysis channels are combined statistically to maximise the sensitivity to the $Wt + \chi\bar{\chi}$ processes.

The final signal regions for the $\mathrm{tW}_{1\mathrm{L}}$ and $\mathrm{tW}_{2\mathrm{L}}$ channels are defined based on a range of discriminating variables including jet and b-jet multiplicities, $E_{\mathrm{T}}^{\mathrm{miss}}$, and (s)transverse mass variables. The dominant SM background contributions in the $\mathrm{tW}_{1\mathrm{L}}$ channel are $t\bar{t}$, W+jets, and single top (Wt channel) production, while in the $\mathrm{tW}_{2\mathrm{L}}$ channel the dominant background processes are $t\bar{t}$, $t\bar{t}Z$, and tWZ production. Background contributions are determined from simulation, and additional control regions are defined to estimate the contribution from the major SM background processes in the signal regions.

No significant excess above the SM is observed in any of the signal regions, thus exclusion limits for the different parameters scans listed in Section 2 have been derived. These exclusion contours are included in the summary plots shown in Section 6.

4.5 $H^{\pm}tb$

This search targets the production of heavy charged Higgs bosons $H^{\pm}$ with masses in the range 0.2–2.0 TeV in association with a top and a bottom quark. The charged Higgs boson decays to a top and a bottom quark, $H^{\pm}(tb)tb$ [29].

Events are required to contain exactly one electron or muon and at least five jets, at least three of which must be b-tagged. The selected events are categorised into four separate regions according to the number of reconstructed jets (j) in an event and number of b-jets (b) among them, referred to as 5j3b, 5j≥4b, ≥6j3b, and ≥6j≥4b. To enhance the separation between signal and background, a neural network is used. The output distributions of the neural network are used in a fit to extract the amount of $H^{\pm}(tb)tb$ signal in data.

The dominant background for this search is composed of $t\bar{t}$ + jets events, including $t\bar{t}$ + light, $t\bar{t} + \geq 1b$ and $t\bar{t} + \geq 1c$, as well as Wt single-top contributions, which are modelled using MC simulations. Data-driven corrections obtained in an additional ≥5j2b region are applied to the simulation.

No significant excess above the expected SM background is observed in any of the signal regions. Hence both model-independent upper limits on the cross section times branching ratio for the signal process as well as model-dependent exclusion contours on specific benchmarks, including a type-II 2HDM in the alignment limit without DM, have been derived [29]. These results can be straightforwardly reinterpreted in the context of the 2HDM+a as the production and decay modes, cross sections and branching ratios of the charged Higgs bosons are identical in both models. This has been verified by comparing the simulated predictions of the 2HDM and 2HDM+a benchmarks for a range of relevant kinematic variables.

4.6 Combination of searches for invisible Higgs boson decays

Searches for invisible Higgs boson decays, $h(\text{inv})$ [46], are also sensitive to the 2HDM+a, which predicts invisible decays of the lighter scalar h to dark matter, $h \to aa^{(*)} \to \chi\bar{\chi}\chi\bar{\chi}$. A preliminary combination for invisible decays of the SM Higgs boson has been performed, based on the results from three searches: a search for invisible decays of the Higgs boson in the VBF topology [47]; a search for invisible decays of the Higgs boson in the $t\bar{t}h$ topology (0ℓ and 2ℓ channels) [48, 49]; the combination of Run-1 searches for invisible Higgs boson decays [50]. An upper limit on the $h \to$ invisible branching ratio of 0.11 $\left(0.11^{+0.04}_{-0.03}\right)$ at 95% confidence level (CL) is observed (expected) [46]. This upper limit is used directly to determine the excluded parameter regions in the 2HDM+a based on the predicted $h \to \chi\bar{\chi}$ branching ratio for each point in the benchmark scans in Section 2.

5 Statistical combination of the $E_{\mathrm{T}}^{\mathrm{miss}} + h(b\bar{b})$ and $E_{\mathrm{T}}^{\mathrm{miss}} + Z(\ell^+\ell^-)$ searches

A statistical combination of two DM searches, $E_{\mathrm{T}}^{\mathrm{miss}} + Z(\ell^+\ell^-)$ and $E_{\mathrm{T}}^{\mathrm{miss}} + h(b\bar{b})$, is described in this section. The $E_{\mathrm{T}}^{\mathrm{miss}}$+$Z$ and $E_{\mathrm{T}}^{\mathrm{miss}}$+$h$ channels are the most sensitive among a variety of $E_{\mathrm{T}}^{\mathrm{miss}}$+$X$ searches and they cover complementary regions of the 2HDM+a parameter space.

To achieve a bias-free statistical combination, it is vital that the two input analyses are statistically independent. The $E_{\mathrm{T}}^{\mathrm{miss}} + Z(\ell^+\ell^-)$ and $E_{\mathrm{T}}^{\mathrm{miss}} + h(b\bar{b})$ analyses are described in Sections 4.1 and 4.2. The signal region (SR) and control region (CR) of the $E_{\mathrm{T}}^{\mathrm{miss}} + Z(\ell^+\ell^-)$ analysis veto the existence of a b-jet, whereas $E_{\mathrm{T}}^{\mathrm{miss}} + h(b\bar{b})$ requires at least one b-jet. Therefore, there is no overlap events between the two analyses. This has been tested by checking all simulated data samples for events passing both analysis selections. None were found, confirming the orthogonality of the two analyses.

5.1 Statistical Analysis Setup

In the combined likelihood fit, the parameter of interest is the signal strength of the 2HDM+a signals, which is implemented as an overall global scaling of all the 2HDM+a processes in the various analyses. The fit model also includes nuisance parameters (NPs) which are floated in the fit but are not of interest for the 2HDM+a measurements. NPs determined from data only are referred to as *unconstrained*. Other NPs, which use information from *auxiliary* measurements, are *constrained* and quantify the effect of systematic uncertainties in the measurement. A unit-Gaussian constraint is assumed for each constrained NP. The mean of the Gaussian is the *global observable* representing the observed value of the auxiliary measurement. When the same systematic uncertainty source affects two channels, the corresponding NPs between them are treated as a single parameter [51]. However, if it is not correlated between the two channels, it is treated as two separate parameters.

The likelihood used in the combined fit is given by [52]

$$\mathcal{L}(\text{data}|\mu, \boldsymbol{\theta}) = \prod_{c=1}^{N_{\text{cats}}} \mathcal{L}_c(\text{data}|\mu, \boldsymbol{\theta}) \prod_{k=1}^{N_{\text{cons}}} \mathcal{F}(\tilde{\theta}_k|\theta_k) \tag{1}$$

where μ is the parameter of interest, $\boldsymbol{\theta}$ is the vector of nuisance parameters (NPs), N_{cats} is the number of categories, N_{cons} is the number of constrained NPs, $\tilde{\theta}_k$ is the global observable corresponding to θ_k, c

runs over categories, k runs over constrained NPs, and $\mathcal{F}$ denotes a Poisson, a Gaussian or a Log-normal distribution depending on the type of uncertainty. The categories represent signal regions and control regions in the fit. The likelihood for a category is a product of Poisson distributions (P):

$$\mathcal{L}_c(\text{data}|\mu, \boldsymbol{\theta}) = \prod_{i=1}^{N_{\text{bins}}} P\left(n_i| \sum_s N_{S_s}(\mu, \boldsymbol{\theta}) + \sum_b N_{B_b}(\boldsymbol{\theta})\right), \tag{2}$$

where N_{bins} is the number of bins, n_i is the observed number of data events in each bin, $\sum\limits_s N_{S_s}(\mu, \boldsymbol{\theta})$ is the signal yield and $\sum\limits_b N_{B_b}(\boldsymbol{\theta})$ is the background yield.

The 95% CL limits are determined using the CLs frequentist formalism [53] with the profile likelihood ratio test statistic [54] implemented using RooStats [55] and RooFit [56].

5.2 Uncertainties and their correlations

5.2.1 Uncertainty correlation scheme

The correlations of uncertainties between $E_{\text{T}}^{\text{miss}} + Z(\ell^+\ell^-)$ and $E_{\text{T}}^{\text{miss}} + h(b\bar{b})$ measurements are determined as follows.

The experimental uncertainties are related to the reconstruction of the objects, such as electrons, muons and jets, by the detector. The electron and muon related uncertainties as well as the $E_{\text{T}}^{\text{miss}}$-related uncertainties are correlated [46, 57]. The b-tagging related uncertainties are uncorrelated because different tagging methods are used. The jet energy scale related uncertainties are correlated because both analyses use the same uncertainty scheme. For uncertainties related to the jet energy resolution, three different correlation scenarios for the corresponding NPs (fully correlated, uncorrelated, anti-correlated) have been compared. The differences between them were found to be negligible. The uncertainties are kept uncorrelated in the final fit.

The theory uncertainties are related to the simulations of background and signal events. The composition and origin of the leading backgrounds are quite different. Also, some backgrounds are estimated via fully data-driven techniques and others are constrained through a series of dedicated and analysis-specific control regions. The sets of NPs used to implement the background modelling uncertainties are significantly different and so is, in part, the phase space considered by the analyses. For these reasons, uncertainties related to background simulations are taken to be uncorrelated.

The $E_{\text{T}}^{\text{miss}} + Z(\ell^+\ell^-)$ and $E_{\text{T}}^{\text{miss}} + h(b\bar{b})$ signal simulations are performed for the two different final states and the signal regions probe very different regions of phase space. Given the fact that all the signal modelling uncertainties in the $E_{\text{T}}^{\text{miss}} + h(b\bar{b})$ measurement are negligible and hence are not included in the statistical analysis, those uncertainties are considered to be uncorrelated.

5.2.2 Impact of uncertainties

The contributions of the statistical and systematic uncertainties on the total uncertainty of the best-fit signal strength for $m_a = 350$ GeV, $m_H = 1$ TeV, $\tan\beta = 1.0$ and $\sin\theta = 0.35$ are shown in Table 1. The total uncertainty is dominated by the statistical uncertainty. The systematic uncertainty is split into four categories for different groups of nuisance parameters: theory, experimental, MC statistical uncertainties, and background normalisation factors. The background normalisation factors are floated in the simultaneous fit of the signal and control regions. They are highly correlated to other systematic uncertainties. The uncertainty for each category is estimated by fixing a group of NPs in a fit and subtracting the resulting uncertainty on the signal strength from the total uncertainty in quadrature. The theoretical uncertainty on the background and signal modelling is found to have the largest impact. The experimental uncertainty is further broken down into the uncertainties related to the different reconstructed objects. The systematic uncertainties related to hadronic jets and flavour tagging are found to be the dominant experimental uncertainties. However they are only small components of the total uncertainty.

Uncertainty source	$\Delta\mu$
Statistical uncertainty	0.11
Systematic uncertainties	0.071
Theory uncertainties	0.046
Experimental uncertainties	0.036
Jets	0.028
$E_{\mathrm{T}}^{\mathrm{miss}}$	0.005
Flavour tagging	0.012
Electrons	0.007
Muons	0.012
Luminosity, pile-up	0.004
MC statistical uncertainty	0.031
Free background normalisation factors	0.021
Total uncertainty	0.13

Table 1: Summary of the absolute uncertainties and their impact on the best-fit signal strength from observed data, obtained by fixing the corresponding nuisance parameters to their best fit values, and subtracting the resulting uncertainty from the total uncertainty in quadrature. The statistical uncertainty component is obtained by fixing all nuisance parameters to their best-fit values. The fitted signal is at $m_a = 350$ GeV, $m_H = 1$ TeV, $\tan\beta = 1.0$ and $\sin\theta = 0.35$.

5.3 Combined Results

The results of the statistical combination in the 2HDM+a DM interpretation are shown in this section. The main purposes of the following plots are to show how the combination improves the expected and observed exclusions and the size of the 1σ and 2σ bands on the expected limit. The features in the shape of the limit contours are further discussed in Section 6.

An interpolation strategy based on linear Radial Basis Functions [58, 59] is used to obtain the continuous exclusion contours based on the discrete set of available signal points for which the exclusion limits have been calculated. The same strategy is used for the $E_{\mathrm{T}}^{\mathrm{miss}} + Z(\ell^+\ell^-)$, $E_{\mathrm{T}}^{\mathrm{miss}} + h(b\bar{b})$ and combination contours.

m_A-m_a scan

Figure 3 shows the exclusion contour for the m_A-m_a scan with both $\sin\theta = 0.35$ and $\sin\theta = 0.7$ (scans 1a and 1b). The regions contained within the observed contours are excluded by the $E_{\mathrm{T}}^{\mathrm{miss}} + h(b\bar{b})$ and $E_{\mathrm{T}}^{\mathrm{miss}} + Z(\ell^+\ell^-)$ combination. For the scan 1a, the exclusion power in terms of m_A and m_a is improved by the combination. The sensitivity at lower values of m_A is mainly driven by the $E_{\mathrm{T}}^{\mathrm{miss}} + Z(\ell^+\ell^-)$ channel. For the scan 1b, the sensitivity improvement from the statistical combination significantly increases the exclusion power at $m_A \simeq 1.0$ - 1.3 TeV. The dashed area indicates the region where the width of any of the Higgs bosons exceeds 20% of its mass. This area indicates a potential increase of modelling uncertainties, however it does not necessarily mean that the model is invalid.

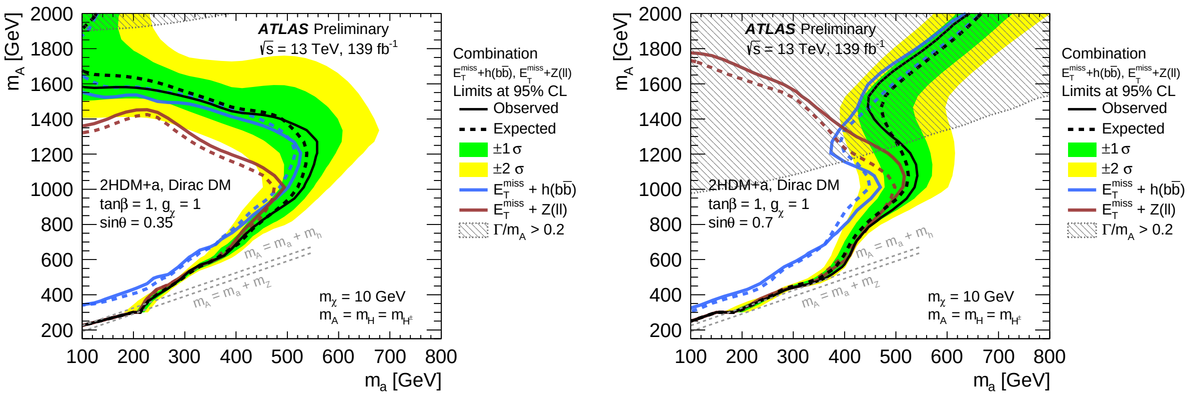

(a)

(b)

Figure 3: Observed (solid lines) and expected (dashed lines) exclusion regions at the 95% CL in the (m_a, m_A) plane under the assumption of (a) $\sin\theta = 0.35$ (scan 1a) and (b) $\sin\theta = 0.7$ (scan 1b). The results are shown for the individual $E_{\mathrm{T}}^{\mathrm{miss}} + Z(\ell^+\ell^-)$ and $E_{\mathrm{T}}^{\mathrm{miss}} + h(b\bar{b})$ searches as well as for their combination. The surrounding green and yellow bands correspond to 1 and 2 standard deviations around the combined expected limits. The grey dashed regions indicate the region where the width of any of the Higgs bosons exceeds 20% of its mass.

$\tan\beta$-m_A scan

Figure 4 shows the exclusion contour for the $\tan\beta$-m_A scan with both $\sin\theta = 0.35$ and $\sin\theta = 0.7$ (scans 2a and 2b). The excluded regions are in the centre of the plots for $E_{\mathrm{T}}^{\mathrm{miss}} + Z(\ell^+\ell^-)$ and $E_{\mathrm{T}}^{\mathrm{miss}} + h(b\bar{b})$ for the scan 2b, while the low and high $\tan\beta$ regions are excluded for $E_{\mathrm{T}}^{\mathrm{miss}} + h(b\bar{b})$ for the scan 2a. The contour is affected by the interplay between gg-fusion and $b\bar{b}$-induced signal processes; the coupling of $H/A/a$ to top quarks (present in gg-fusion production) is proportional to $\cot\beta$, while the coupling to bottom quarks is proportional to $\tan\beta$. For this reason, gg processes dominate for $\tan\beta < 1$. Signals with large cross sections are easier to exclude, hence the contour is wider in the lower $\tan\beta$ region for both $E_{\mathrm{T}}^{\mathrm{miss}} + Z(\ell^+\ell^-)$ and $E_{\mathrm{T}}^{\mathrm{miss}} + h(b\bar{b})$. As $\tan\beta$ increases, the gg cross section decreases and the contour narrows; eventually the $b\bar{b}$ contribution becomes significant and the cross section grows, causing the contour to widen ($E_{\mathrm{T}}^{\mathrm{miss}} + Z(\ell^+\ell^-)$) or appear again ($E_{\mathrm{T}}^{\mathrm{miss}} + h(b\bar{b})$) at high $\tan\beta$. Samples with $\sin\theta = 0.35$ have higher cross sections at high $\tan\beta$ than the ones with $\sin\theta = 0.7$; likewise, samples with $\sin\theta = 0.7$ have higher cross sections at low $\tan\beta$ than the ones with $\sin\theta = 0.35$. This leads to a better exclusion in the scan 2a at high tan β [1], and in the scan 2b at low tan β . The sensitivity improvement from the combination is clear for tan β values around 1–5.

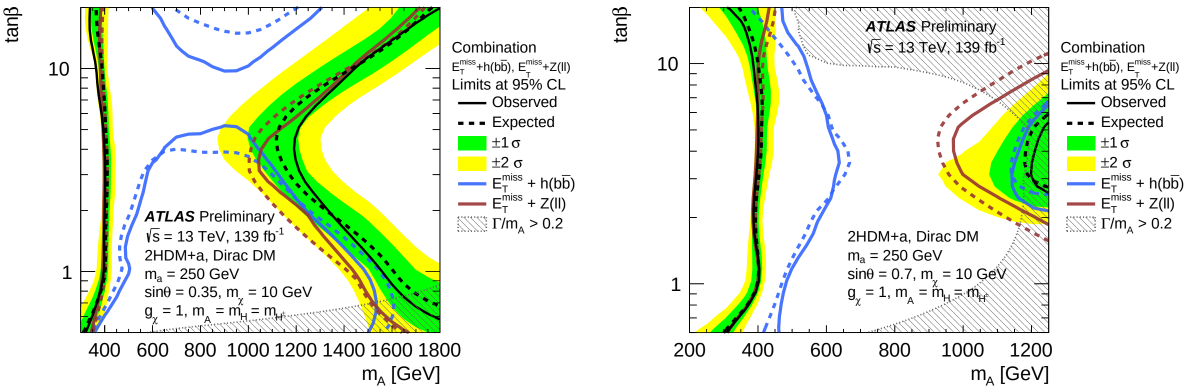

(a)

(b)

Figure 4: Observed (solid lines) and expected (dashed lines) exclusion regions at the 95% CL in the $(m_A, \tan\beta)$ plane under the assumption of (a) $\sin\theta = 0.35$ (scan 2a) and (b) $\sin\theta = 0.7$ (scan 2b). The results are shown for the individual $E_{\mathrm{T}}^{\mathrm{miss}} + Z(\ell^+\ell^-)$ and $E_{\mathrm{T}}^{\mathrm{miss}} + h(b\bar{b})$ searches as well as for their combination. The surrounding green and yellow bands correspond to 1 and 2 standard deviations around the combined expected limits. The dashed grey regions indicate the region where the width of any of the Higgs bosons exceeds 20% of its mass.

tan β-m_a scan

Figure 5 shows the exclusion contour for the tan β-m_a scan with both $\sin\theta = 0.35$ and $\sin\theta = 0.7$ (scans 3a and 3b). The excluded regions are the left-hand side areas of the plots. For $E_{\mathrm{T}}^{\mathrm{miss}} + h(b\bar{b})$, the shapes of these limit contours again depend strongly on the relative contributions from gg- and $b\bar{b}$-initiated production to the total production cross section, while this effect is less significant for $E_{\mathrm{T}}^{\mathrm{miss}} + Z(\ell^+\ell^-)$. The combined sensitivity is mainly driven by the $E_{\mathrm{T}}^{\mathrm{miss}} + Z(\ell^+\ell^-)$ channel. The dashed area indicates the region where the width of any of the Higgs bosons exceeds 20% of its mass.

sin θ scan

Figure 6 shows the exclusion limits as a function of sin θ for the 2HDM+a model, following the two parameter choices (scans 4a and 4b) described in Section 2. The $E_{\mathrm{T}}^{\mathrm{miss}} + h(b\bar{b})$ search reaches its maximum sensitivity around $\sin\theta = 0.5$ because the non-resonant and resonant production for $E_{\mathrm{T}}^{\mathrm{miss}} + h(b\bar{b})$ have different trends as a function of sin θ , while for $E_{\mathrm{T}}^{\mathrm{miss}} + Z(\ell^+\ell^-)$ both of the productions tend to monotonically increase. For the low-mass scan (left plot), the sensitivity is driven by the $E_{\mathrm{T}}^{\mathrm{miss}} + Z(\ell^+\ell^-)$ search. For the high-mass scan (right plot), a good complementary coverage is found and the combination significantly improves the sensitivity. Almost the whole range is excluded in both low-mass and high-mass sin θ scans.

m_χ scan

Figure 7 shows the exclusion limits as a function of the DM mass m_χ for the 2HDM+a benchmark, following the parameter choices of scan 5.

---

[1] Note that the $\sin\theta = 0.7$ scan in Figure 4 is truncated at $m_A = 1.225$ TeV

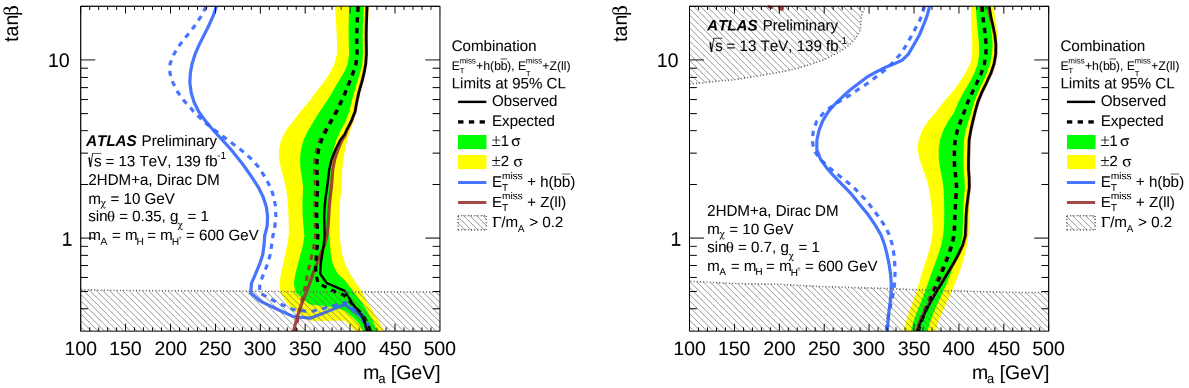

(a) (b)

Figure 5: Observed (solid lines) and expected (dashed lines) exclusion regions at the 95% CL in the $(m_a\,, \tan\beta)$ plane under the assumption of (a) $\sin\theta = 0.35$ (scan 3a) and (b) $\sin\theta = 0.7$ (scan 3b). The results are shown for the individual $E_{\mathrm{T}}^{\mathrm{miss}} + Z(\ell^+\ell^-)$ and $E_{\mathrm{T}}^{\mathrm{miss}} + h(b\bar{b})$ searches as well as for their combination. The surrounding green and yellow bands correspond to 1 and 2 standard deviations around the combined expected limits.

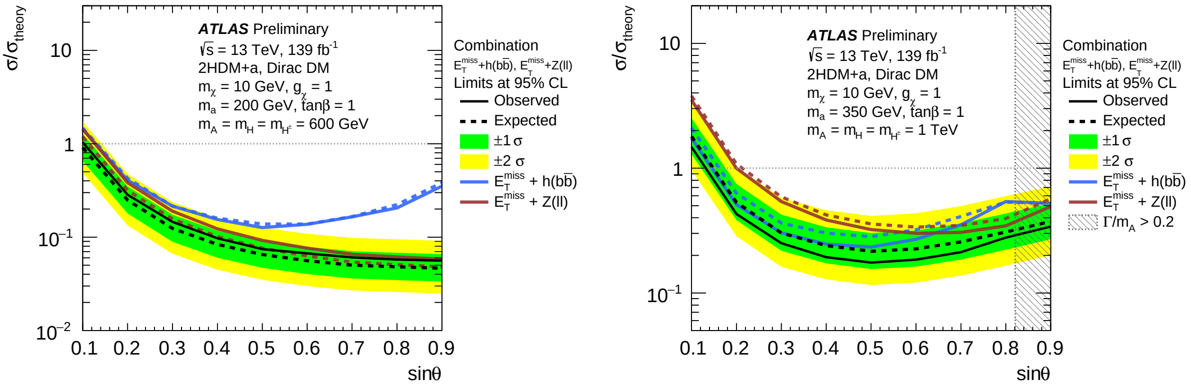

(a) (b)

Figure 6: Observed (solid lines) and expected (dashed lines) exclusion limits at 95% CL for the 2HDM+a model as a function of $\sin\theta$, for $\tan\beta = 1.0$ and (a) $m_A = 0.6$ TeV , $m_a = 200$ GeV (scan 4a: low-mass hypothesis) and (b) $m_A = 1.0$ TeV , $m_a = 350$ GeV (scan 4b: high-mass hypothesis). The results are shown for the individual $E_{\mathrm{T}}^{\mathrm{miss}} + Z(\ell^+\ell^-)$ and $E_{\mathrm{T}}^{\mathrm{miss}} + h(b\bar{b})$ searches as well as for their combination. The surrounding bands correspond to 1 and 2 standard deviations around the combined expected limits.

For both $E_{\mathrm{T}}^{\mathrm{miss}} + Z(\ell^{+}\ell^{-})$ and $E_{\mathrm{T}}^{\mathrm{miss}} + h(b\bar{b})$ analyses, the sensitivity is independent of the DM mass as long as the lightest pseudoscalar mediator, whose mass is fixed at 250 GeV in this scan, is kinematically allowed to decay into a $\chi\chi$ pair. Both $E_{\mathrm{T}}^{\mathrm{miss}} + Z(\ell^{+}\ell^{-})$ and $E_{\mathrm{T}}^{\mathrm{miss}} + h(b\bar{b})$ analyses exclude this parameter space. For higher DM masses, the sensitivity of the two analyses and the combination quickly decreases and no exclusion is observed. The combination slightly improves the sensitivity across the whole range compared to the individual searches.

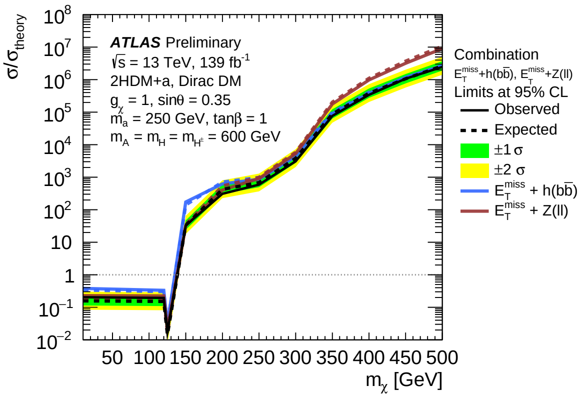

Figure 7: Observed (solid lines) and expected (dashed lines) exclusion limits for the 2HDM+*a* model as a function of m_{χ}, following the parameter choices of $m_A = 0.6$ TeV, $m_a = 250$ GeV, $\tan\beta = 1.0$ and $\sin\theta = 0.35$ (scan 5). The limits are calculated at 95% CL and are expressed in terms of the ratio of the excluded cross section to the nominal cross section of the model. The results are shown for the individual $E_{\mathrm{T}}^{\mathrm{miss}} + Z(\ell^{+}\ell^{-})$ and $E_{\mathrm{T}}^{\mathrm{miss}} + h(b\bar{b})$ searches as well as for their combination. The features of the curves shown in this plot are discussed in more detail in Section 6.

6 Summary of constraints on the 2HDM+a benchmark

In the following, the constraints on the 2HDM+a derived from the searches described in Section 4 and the combination in Section 5 are presented in terms of the benchmark scans discussed in Section 2. The $E_{\mathrm{T}}^{\mathrm{miss}} + Z(\ell^+\ell^-)$, $E_{\mathrm{T}}^{\mathrm{miss}} + h(b\bar{b})$ and combination contours are drawn with the same interpolation method for consistency between them.

m_A-m_a scan

Figure 8 shows the exclusion contours for the m_A-m_a scans with both $\sin\theta = 0.35$ and $\sin\theta = 0.7$, which correspond to benchmark scans 1a and 1b in Section 2. The $E_{\mathrm{T}}^{\mathrm{miss}} + Z(\ell^+\ell^-)$ and $E_{\mathrm{T}}^{\mathrm{miss}} + h(b\bar{b})$ searches dominate the sensitivity across the two parameter planes, which is largely due to the resonant production of the (pseudo)scalars according to the diagram in Figure 2(e). Their sensitivities depend on both pseudoscalar Higgs and mediator masses. For scan 1a, the maximum reach is obtained for m_a up to 560 GeV, if the A-boson mass is set to 1.2 TeV, while for $m_a = 150$ GeV A-boson masses between 250 GeV and 1.55 TeV are excluded. In both scans, but most notably for scan 1b, an increase in the exclusion power of the $E_{\mathrm{T}}^{\mathrm{miss}} + h$ searches is observed at larger values of m_A and low values of m_a. This is due to an increase of the cross section of the $a \to ah$ process, without resonant A production. No equivalent process exists for the $E_{\mathrm{T}}^{\mathrm{miss}}$+$Z$ signature. In this context, it is worth noting that, given the current parameter choices for the 2HDM+a (Section 2), the aah coupling exceeds 4π for $m_A \gtrsim 1.75$ TeV. Furthermore, values of $m_A \gtrsim 1.25$ TeV are not consistent with the requirement of having a bounded-from-below scalar potential. These constraints, however, can be relaxed substantially if the quartic couplings take a value closer to the perturbativity limit and also in more general 2HDMs containing additional couplings as discussed in Refs. [21, 22, 60]. Hence the above considerations should not be understood as strong limitations on the validity of the model predictions that were used to derive the above exclusion contours. Finally, it is to be noted that for high m_A the width of the additional heavy Higgs bosons grows substantially and the theoretical predictions are subject to additional theoretical uncertainties associated with the treatment of the width. This is indicated by the grey shaded area marking the region where the relative width Γ/m of at least one of the heavy Higgs bosons exceeds 20%.

In the lower left area, the $E_{\mathrm{T}}^{\mathrm{miss}} + Z(\ell^+\ell^-)$ limit reaches the $m_A = m_a + m_h$ line while the $E_{\mathrm{T}}^{\mathrm{miss}} + h(b\bar{b})$ limit does not. This is because $E_{\mathrm{T}}^{\mathrm{miss}} + Z(\ell^+\ell^-)$ can probe lower $E_{\mathrm{T}}^{\mathrm{miss}}$ space, whereas $E_{\mathrm{T}}^{\mathrm{miss}} + h(b\bar{b})$ requires a higher $E_{\mathrm{T}}^{\mathrm{miss}}$ threshold due to the use of a $E_{\mathrm{T}}^{\mathrm{miss}}$ trigger.

In addition to the $E_{\mathrm{T}}^{\mathrm{miss}} + Z(\ell^+\ell^-)$ results, the observed and expected exclusion contours from a $E_{\mathrm{T}}^{\mathrm{miss}}$+$V(q\bar{q})$ search on 36 fb^{-1}of $\sqrt{s} = 13$ TeV pp collision data [61] are shown for the scan 1a. This result was already included in Ref. [23]. The sensitivity of this search is considerably smaller than that of the $E_{\mathrm{T}}^{\mathrm{miss}} + Z(\ell^+\ell^-)$ search due to the larger backgrounds from strong multijet production in the hadronic decay channel.

The $E_{\mathrm{T}}^{\mathrm{miss}}$+$Wt$ search probes a similarly shaped, albeit smaller, region in parameter space compared to the $E_{\mathrm{T}}^{\mathrm{miss}} + Z(\ell^+\ell^-)$ in scan 1b. Its observed exclusion is weaker than the expected sensitivity due to a small (within 2σ) excess in the $tW_{2\mathrm{L}}$ region [28]. Exclusion contours for the $E_{\mathrm{T}}^{\mathrm{miss}}$+$Wt$ search are only shown for the scan 1b where the sensitivity of the search is larger compared to the scan 1a [31].

The $H^{\pm}(tb)tb$ search provides complementary sensitivity to the $E_{\mathrm{T}}^{\mathrm{miss}} + X$ searches. Its exclusion contour shows only a moderate dependence on m_a as this search does not probe the production of the pseudoscalar mediator directly and is therefore only indirectly affected by the choice of m_a via its effect on the relative branching ratio to tb compared to the branching ratios for other possible decay modes, such as $H^{\pm} \to aW^{\pm}, AW^{\pm}, HW^{\pm}$.

Finally, the limit on the branching ratio for invisible Higgs boson decays constrains very low values of m_a, as searches for invisible Higgs boson decays are sensitive only to the a boson production cross section.

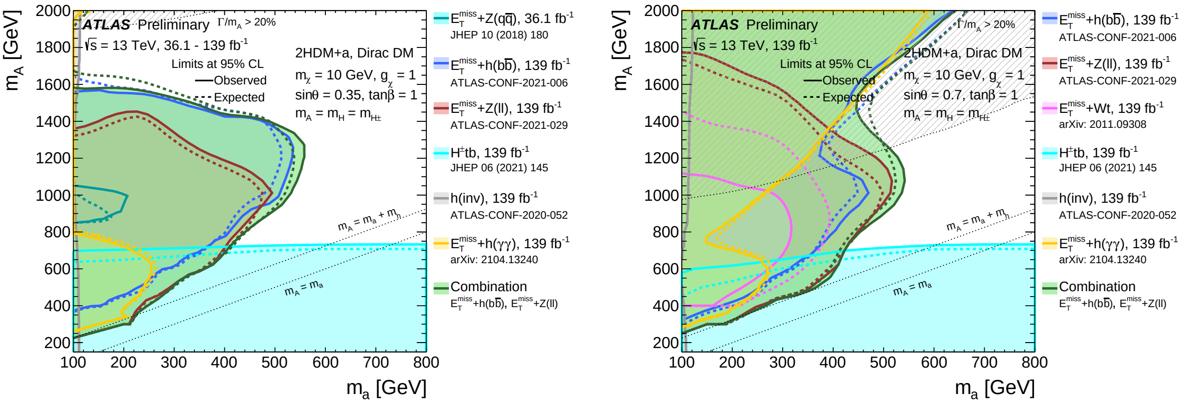

(a)

(b)

Figure 8: Observed (solid lines) and expected (dashed lines) exclusion regions at 95% CL in the (m_a, m_A) plane under the assumption of (a) $\sin\theta = 0.35$ (scan 1a) and (b) $\sin\theta = 0.7$ (scan 1b). The results are shown for several individual searches as well as the combination of the $E_T^{miss} + Z(\ell^+\ell^-)$ and $E_T^{miss} + h(b\bar{b})$ searches. The dashed grey regions indicate the region where the width of any of the Higgs bosons exceeds 20% of its mass. The larger exclusions of $E_T^{miss} + h(b\bar{b})$ and $E_T^{miss} + h(\gamma\gamma)$ in high m_A region are due to an increase of the cross section of the $a \rightarrow ah$ process, which are more significant when $\sin\theta = 0.7$.

$\tan\beta$ -m_A scan

In the context of 2HDM interpretations, it is customary and well motivated to show exclusion contours in terms of the mass of the pseudoscalar A and $\tan\beta$. This parameterisation is described by benchmark scan 2 introduced in Section 2, which is conducted for both $\sin\theta = 0.35$ (scan 2a) and $\sin\theta = 0.7$ (scan 2b). The results are shown in Figure 9.

In the case of scan 2a, the probed parameter space is almost fully excluded by the $E_T^{miss} + Z(\ell^+\ell^-)$ search alone. The situation is similar for the scan 2b, except that in this case, the $E_T^{miss} + Wt$ search also probes the low $\tan\beta$ region for large values of m_A.

In scan 2a, the $E_T^{miss} + h(b\bar{b})$ loses sensitivity in the lower $\tan\beta$ and higher m_A region. This is due to the rapid change of the production cross sections in this area.

The E_T^{miss}+Wt search probes a low $\tan\beta$ region in parameter space compared to the $E_T^{miss} + Z(\ell^+\ell^-)$ search for scan 2b. Its observed exclusion is weaker than the expected sensitivity due to a small (within 2σ) excess in the tW_{2L} region [28]. Again, exclusion contours for the E_T^{miss}+Wt search are only shown for the scan 2b where the sensitivity of the search is larger compared to the scan 2a [31]. Furthermore, no exclusion contours are shown for the E_T^{miss}+$h(\gamma\gamma)$ search.

The $H^{\pm}tb$ search provides complementary sensitivity to the $E_T^{miss} + X$ searches. It has a moderate m_A dependence in the lower m_A region.

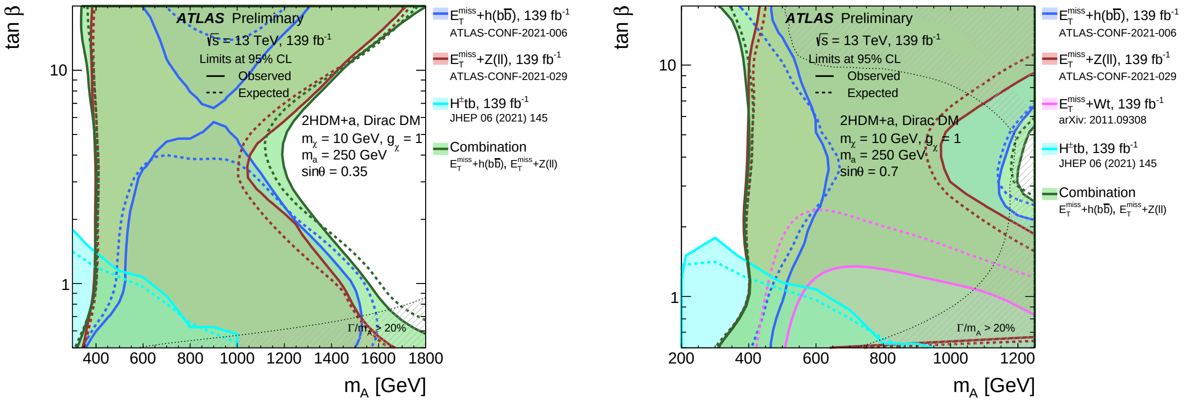

(a) (b)

Figure 9: Observed (solid lines) and expected (dashed lines) exclusion regions at 95% CL in the $(m_A, \tan\beta)$ plane under the assumption of (a) $\sin\theta = 0.35$ (scan 2a) and (b) $\sin\theta = 0.7$ (scan 2b). The results are shown for several individual searches as well as the combination of the $E_{\mathrm{T}}^{\mathrm{miss}} + Z(\ell^+\ell^-)$ and $E_{\mathrm{T}}^{\mathrm{miss}} + h(b\bar{b})$ searches. The dashed grey regions indicate the region where the width of any of the Higgs bosons exceeds 20% of its mass.

$\tan\beta$ -m_a scan

Figure 10 shows a similar scan to the one in Figure 9 but this time varying the mass of the pseudoscalar mediator m_a rather than m_A (benchmark scan 3 in Section 2). Again, the exclusion contours are shown for both $\sin\theta = 0.35$ (scan 3a) and $\sin\theta = 0.7$ (scan 3b). The strongest exclusion is observed from the $E_{\mathrm{T}}^{\mathrm{miss}} + Z(\ell^+\ell^-)$ and $E_{\mathrm{T}}^{\mathrm{miss}} + h(b\bar{b})$ searches. In both cases, an increase in the exclusion range in terms of m_a is found for large values of $\tan\beta$, compared to a weaker exclusion around $\tan\beta = 3$ ($\tan\beta = 8$ for $E_{\mathrm{T}}^{\mathrm{miss}} + h(b\bar{b})$ in scan 3a). This increase is due to the contributions from $b\bar{b}$-initiated signal production, which becomes dominant at large values of $\tan\beta$. The exclusion contours for the $E_{\mathrm{T}}^{\mathrm{miss}}+h$ searches show a different $\tan\beta$ dependence than the one for $E_{\mathrm{T}}^{\mathrm{miss}} + Z(\ell^+\ell^-)$, in particular for scan 3b, with a notable reduction in the sensitivity for $\tan\beta \simeq 3-5$. This is due to a reduction in the overall production cross section for the $E_{\mathrm{T}}^{\mathrm{miss}}+h$ signature that is not present for the $E_{\mathrm{T}}^{\mathrm{miss}} + Z$ signature.

The $E_{\mathrm{T}}^{\mathrm{miss}} + h(b\bar{b})$ sensitivity increases at lower $\tan\beta$ in scan 3a because its cross section is proportional to $\cot^2\beta$ and rapidly increases as $\tan\beta$ decreases in this region.

No exclusion contours from the $E_{\mathrm{T}}^{\mathrm{miss}}+Wt$ search are shown for the $\tan\beta$-m_a scans. For the scan with $\sin\theta = 0.35$, results from searches for $E_{\mathrm{T}}^{\mathrm{miss}}$ in association with a $t\bar{t}$ pair are included [62, 63]. These searches are sensitive to the $t\bar{t}$-associated production of the mediator a and its subsequent decay to $\chi\bar{\chi}$. The combined exclusion contour, which was already included in Ref. [23], is based on 36 fb^{-1}of $\sqrt{s} = 13$ TeV pp collision data and excludes very small values of $\tan\beta$ in the region characterised by large Higgs boson widths.

The $H^{\pm}tb$ search provides complementary sensitivity to the $E_{\mathrm{T}}^{\mathrm{miss}} + X$ searches. As in the m_A-m_a scan (Figure 8), the exclusion contour shows only a moderate dependence on m_a.

Additionally, results from a search for new phenomena in a lepton plus high jet multiplicity final state [64] consistent with four-top-quark ($t\bar{t}t\bar{t}$) production are shown for the case $\sin\theta = 0.35$. It is sensitive to the $t\bar{t}$-associated production of the neutral particles a, A, or H and their subsequent decay to $t\bar{t}$. Its exclusion contours, which were already included in Ref. [23], are derived based on 36 fb^{-1}of $\sqrt{s} = 13$ TeV pp

collision data and show a similar dependence on m_a as those from the $H^{\pm}tb$ search while excluding a smaller $\tan\beta$ range.

Finally, the h(inv) branching ratio limit again provides constraints at very low values of m_a, independent of the value of $\tan\beta$.

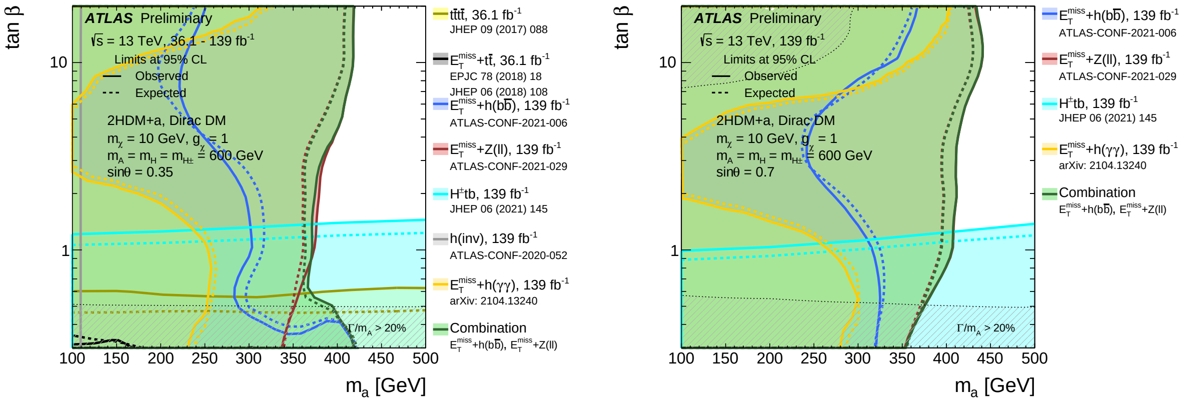

(a)

(b)

Figure 10: Observed (solid lines) and expected (dashed lines) exclusion regions at 95% CL in the $(m_a, \tan\beta)$ plane under the assumption of (a) $\sin\theta = 0.35$ (scan 3a) and (b) $\sin\theta = 0.7$ (scan 3b). The results are shown for several individual searches as well as the combination of the $E_{\mathrm{T}}^{\mathrm{miss}} + Z(\ell^+\ell^-)$ and $E_{\mathrm{T}}^{\mathrm{miss}} + h(b\bar{b})$ searches. The dashed grey regions indicate the region where the width of any of the Higgs bosons exceeds 20% of its mass.

$\sin\theta$ scan

Figure 11 shows the exclusion limits as a function of $\sin\theta$ for the 2HDM+a model for a low-mass and high-mass mediator a hypothesis, following the two parameter choices of scan 4 in Section 2. The limits are expressed in terms of the ratio of the excluded cross section to the nominal cross section of the model.

For scan 4a, the strongest exclusion in the medium $\sin\theta$ range is provided by the $E_{\mathrm{T}}^{\mathrm{miss}} + Z(\ell^+\ell^-)$ and $E_{\mathrm{T}}^{\mathrm{miss}} + h(b\bar{b})$ searches. The sensitivity of the former monotonically improves as a function of $\sin\theta$, as the cross section of the non-resonant and resonant production diagrams, in Figures 1(d) and 1(e), respectively, increases with $\sin\theta$, while the same production diagrams for the $E_{\mathrm{T}}^{\mathrm{miss}}$+$h$ signature have very different $\sin\theta$ dependence in the two scans explored here, as described in Refs. [21, 23]. The $H^{\pm}tb$ signature shows a different $\sin\theta$ dependence compared to the other signatures as it is not directly sensitive to the neutral boson production. It is particularly sensitive at very small mixing angles.

In scan 4b, the mass of the light pseudoscalar is high enough that the decay $a \to t\bar{t}$ is kinematically allowed, which introduces an additional $\sin\theta$ dependence to the $E_{\mathrm{T}}^{\mathrm{miss}} + X$ analyses interpreted in this scan. For this reason, the highest sensitivity for the $E_{\mathrm{T}}^{\mathrm{miss}} + X$ analyses is typically found to be around (or slightly below) the maximal mixing condition ($\theta = \pi/4$). The $E_{\mathrm{T}}^{\mathrm{miss}}$+$h$ signatures, however, have a complex $\sin\theta$ dependence due to the different contributions of resonant and non-resonant processes to the final selection in the two analyses. The sensitivity of the $E_{\mathrm{T}}^{\mathrm{miss}} + h(b\bar{b})$ search exhibits a broad maximum for $\sin\theta$ values below the maximal mixing condition ($\theta = \pi/4$). The $E_{\mathrm{T}}^{\mathrm{miss}} + h(\gamma\gamma)$ search instead shows a local sensitivity minimum around $\sin\theta \simeq 0.6$. The $H^{\pm}tb$ signature, as in scan 4b, shows a constant sensitivity as a function of $\sin\theta$. The $E_{\mathrm{T}}^{\mathrm{miss}} + Wt$ search is not included in this scan.

Again, the results from the $E_{\mathrm{T}}^{\mathrm{miss}}$+$V(q\bar{q})$, $t\bar{t}t\bar{t}$, and $E_{\mathrm{T}}^{\mathrm{miss}}$+$t\bar{t}/b\bar{b}$ searches from Ref. [23] are shown for completeness. The strongest constraints, however, are provided by the searches relying on 139 fb^{-1}of data for all $\sin\theta$ values in both scans.

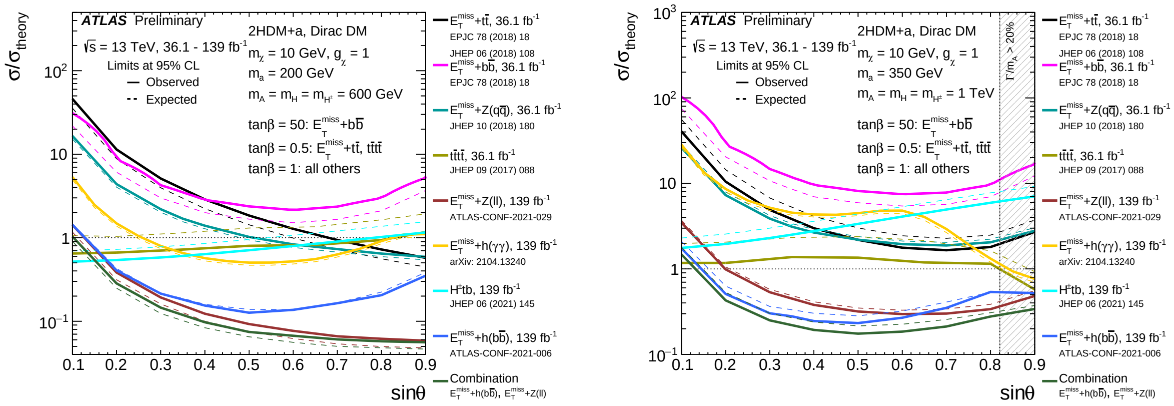

(a)

(b)

Figure 11: Observed (solid lines) and expected (dashed lines) exclusion limits at 95% CL for the 2HDM+a model as a function of $\sin\theta$, for $\tan\beta\ = 1.0$ and (a) $m_A = 0.6$ TeV , $m_a = 200$ GeV (scan 4a: low-mass hypothesis) and (b) $m_A = 1.0$ TeV , $m_a = 350$ GeV (scan 4b: high-mass hypothesis). The results are shown for several individual searches as well as the combination of the $E_{\mathrm{T}}^{\mathrm{miss}} + Z(\ell^+\ell^-)$ and $E_{\mathrm{T}}^{\mathrm{miss}} + h(b\bar{b})$ searches.

m_χ scan

In Figure 12, the experimental reach of the different searches are compared with regard to the DM mass m_χ, which is the parameter with the strongest impact on the relic density predicted by the 2HDM+a. It corresponds to benchmark scan 5 in Section 2. The searches are compared in terms of the observed exclusion limits on the ratio of the excluded cross section to the nominal cross section of the model (left vertical axis) as a function of m_χ.

Again, the results from the $E_{\mathrm{T}}^{\mathrm{miss}}$+$V(q\bar{q})$ as well as a re-interpretation of a $E_{\mathrm{T}}^{\mathrm{miss}}$+$b\bar{b}$ search [62] from Ref. [23] are shown for completeness. The $t\bar{t}t\bar{t}$ search has not been interpreted in the context of this benchmark scan.

The predicted relic density (right vertical axis) for each value of m_χ is overlaid on the plot as a long-dashed line. The two regions at $m_\chi = 125$ GeV and $m_\chi = 300$ GeV marked by light-grey bars correspond to the a-funnel and A-funnel regions [22, 65, 66] where the predicted relic density is depleted by the resonant enhancement of the processes $\chi\bar{\chi} \to A/a \to$ SM. This and other features of the relic density curve are discussed in more detail in Ref. [23] and references therein.

For all signatures shown here, the sensitivity is independent of m_χ as long as the pseudoscalar mediator, whose mass is fixed at 250 GeV in this scan, is allowed to decay into a $\chi\bar{\chi}$ pair. The strongest constraints on this region are provided by the $E_{\mathrm{T}}^{\mathrm{miss}} + Z(\ell^+\ell^-)$ search, which, together with the $E_{\mathrm{T}}^{\mathrm{miss}} + h(b\bar{b})$ search, excludes this parameter space. For higher DM masses, the sensitivity of the $E_{\mathrm{T}}^{\mathrm{miss}}$+$X$ searches quickly decreases. For $m_\chi > m_a/2$, the strongest constraints are obtained from the $H^\pm(tb)tb$ search, which excludes the 2HDM+a for the chosen parameter values for all values m_χ.

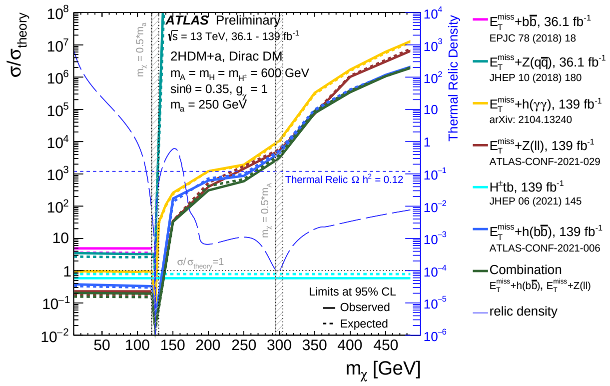

Figure 12: Observed (solid lines) and expected (dashed lines) exclusion limits for the 2HDM+a model as a function of m_χ , following the parameter choices of $m_A = 0.6$ TeV, $m_a = 250$ GeV, $\tan\beta\ = 1.0$ and $\sin\theta = 0.35$ (scan 5). The limits are calculated at 95% CL and are expressed in terms of the ratio of the excluded cross section to the nominal cross section of the model. The results are shown for several individual searches as well as the combination of the $E_{\mathrm{T}}^{\mathrm{miss}} + Z(\ell^+\ell^-)$ and $E_{\mathrm{T}}^{\mathrm{miss}} + h(b\bar{b})$ searches. The relic density for each m_χ assumption is superimposed in the plot (long-dashed line) and described by the right vertical axis. For dark matter mass values where the relic density line is below $\Omega h^2 = 0.12$, the model depletes the relic density to below the thermal value. The two valleys at $m_\chi = 125$ GeV and $m_\chi = 300$ GeV determine the two a-funnel and A-funnel regions [22, 65, 66] where the predicted relic density is depleted by the resonant enhancement of the processes $\chi\bar{\chi} \rightarrow A/a \rightarrow$ SM. The shaded region around 125 GeV indicates a ±5 GeV band around the kinematic thresholds $m_\chi = 0.5 \cdot m_a$ and $m_\chi = 0.5 \cdot m_A$ where the generator results are deemed unreliable. The interpolation of the exclusion limit for the $E_{\mathrm{T}}^{\mathrm{miss}} + h$ and $E_{\mathrm{T}}^{\mathrm{miss}} + Z$ searches in the region 125-150 GeV in m_χ is subject to large uncertainties due to the rapidly changing cross sections in this region.

7 Conclusion

In this note, a variety of different searches for new phenomena performed by the ATLAS Collaboration are summarised and interpreted in the context of a common LHC dark matter benchmark model, namely a Two-Higgs-Doublet-Model with an additional pseudoscalar mediator a (2HDM+a), which couples the dark matter particles to the Standard Model. This model predicts a rich phenomenology of processes resulting in a diverse range of final-state signatures. The searches presented in this note, which target various different detector signatures, provide sensitivity across a wide range of the model parameter space.

All updated analyses are based on 139 fb^{-1} of proton-proton collision data at a centre-of-mass energy of $\sqrt{s} = 13$ TeV collected by the ATLAS detector at the LHC in the years 2015–2018. None of the searches has reported a significant deviation of the data from the predictions of the Standard Model. The results are therefore used to derive exclusion limits on the 2HDM+a benchmark for a representative set of parameter scans.

Masses of the pseudo-scalar mediator a are excluded up to 560 GeV for $m_A = m_H = m_{H^\pm} = 1.2$ TeV, $\sin\theta = 0.35$ and $\tan\beta = 1.0$. The $E_{\text{T}}^{\text{miss}} + Z(\ell^+\ell^-)$ and $E_{\text{T}}^{\text{miss}} + h(b\bar{b})$ searches are the most sensitive analyses in this high mediator-mass region. A statistical combination of these two searches is presented here, which allows to further extend the sensitivity of the search programme in the 2HDM+a parameter space. This is the first time two searches targeting different final-state signatures are statistically combined to provide constraints on the 2HDM+a.

Additionally, results from a new search targeting $E_{\text{T}}^{\text{miss}}+Wt$ final states and a search for charged Higgs bosons $H^\pm$ decaying to tb, which is interpreted for the first time in the context of the 2HDM+a, are shown. The results in this note represent the most comprehensive set of constraints on the 2HDM+a obtained by the ATLAS Collaboration to date.

References

[1] G. Hinshaw et al., *Nine-Year Wilkinson Microwave Anisotropy Probe (WMAP) Observations: Cosmological Parameter Results*, Astrophys. J. Suppl. **208** (2013) 19, arXiv: `1212.5226 [astro-ph.CO]` (cit. on p. 2).

[2] Planck Collaboration, *Planck 2018 results. I. Overview and the cosmological legacy of Planck*, Astron. Astrophys. **641** (2020) A1, arXiv: `1807.06205 [astro-ph.CO]` (cit. on p. 2).

[3] V. Trimble, *Existence and Nature of Dark Matter in the Universe*, Annual Review of Astronomy and Astrophysics **25** (1987) 425 (cit. on p. 2).

[4] G. Bertone, D. Hooper and J. Silk, *Particle dark matter: evidence, candidates and constraints*, Physics Reports **405** (2005) 279, ISSN: 0370-1573, URL: `http://dx.doi.org/10.1016/j.physrep.2004.08.031` (cit. on p. 2).

[5] J. L. Feng, *Dark Matter Candidates from Particle Physics and Methods of Detection*, Annual Review of Astronomy and Astrophysics **48** (2010) 495, ISSN: 1545-4282, URL: `http://dx.doi.org/10.1146/annurev-astro-082708-101659` (cit. on p. 2).

[6] ATLAS Collaboration, *The ATLAS Experiment at the CERN Large Hadron Collider*, JINST **3** (2008) S08003 (cit. on p. 2).

[7] L. Evans and P. Bryant, *LHC Machine*, JINST **3** (2008) S08001,
URL: `https://doi.org/10.1088/1748-0221/3/08/s08001` (cit. on p. 2).

[8] G. Steigman and M. S. Turner,
Cosmological constraints on the properties of weakly interacting massive particles,
Nuclear Physics B **253** (1985) 375, ISSN: 0550-3213,
URL: `https://www.sciencedirect.com/science/article/pii/0550321385905371`
(cit. on p. 2).

[9] ATLAS Collaboration, *Search for new phenomena in events with an energetic jet and missing transverse momentum in pp collisions at* $\sqrt{s} = 13$ *TeV with the ATLAS detector*, (2021), arXiv: `2102.10874 [hep-ex]` (cit. on p. 2).

[10] CMS Collaboration, *Search for new physics in final states with an energetic jet or a hadronically decaying W or Z boson and transverse momentum imbalance at* $\sqrt{s} = 13$ *TeV*, Phys. Rev. D **97** (2018) 092005, arXiv: `1712.02345 [hep-ex]` (cit. on p. 2).

[11] ATLAS Collaboration, *Search for new resonances in mass distributions of jet pairs using* $139\,fb^{-1}$ *of pp collisions at* $\sqrt{s} = 13$ *TeV with the ATLAS detector*, JHEP **03** (2020) 145, arXiv: `1910.08447 [hep-ex]` (cit. on p. 2).

[12] ATLAS Collaboration, *Search for high-mass dilepton resonances using* $139\,fb^{-1}$ *of pp collision data collected at* $\sqrt{s} = 13$ *TeV with the ATLAS detector*, Phys. Lett. B **796** (2019) 68, arXiv: `1903.06248 [hep-ex]` (cit. on p. 2).

[13] CMS Collaboration, *Search for narrow and broad dijet resonances in proton–proton collisions at* $\sqrt{s} = 13$ *TeV and constraints on dark matter mediators and other new particles*, JHEP **08** (2018) 130, arXiv: `1806.00843 [hep-ex]` (cit. on p. 2).

[14] CMS Collaboration, *Search for high mass dijet resonances with a new background prediction method in proton–proton collisions at* $\sqrt{s} = 13$ *TeV*, JHEP **05** (2020) 033, arXiv: `1911.03947 [hep-ex]` (cit. on p. 2).

[15] CMS Collaboration, *Search for resonant and nonresonant new phenomena in high-mass dilepton final states at* $\sqrt{s} = 13$ *TeV*, (2021), arXiv: `2103.02708 [hep-ex]` (cit. on p. 2).

[16] D. Abercrombie et al., *Dark Matter benchmark models for early LHC Run-2 Searches: Report of the ATLAS/CMS Dark Matter Forum*, Phys. Dark Univ. **27** (2020) 100371, ed. by A. Boveia, C. Doglioni, S. Lowette, S. Malik and S. Mrenna, arXiv: `1507.00966 [hep-ex]` (cit. on p. 2).

[17] A. Boveia et al., *Recommendations on presenting LHC searches for missing transverse energy signals using simplified s-channel models of dark matter*, Phys. Dark Univ. **27** (2020) 100365, ed. by O. Buchmueller et al., arXiv: `1603.04156 [hep-ex]` (cit. on p. 2).

[18] A. Albert et al., *Recommendations of the LHC Dark Matter Working Group: Comparing LHC searches for dark matter mediators in visible and invisible decay channels and calculations of the thermal relic density*, Phys. Dark Univ. **26** (2019) 100377, arXiv: `1703.05703 [hep-ex]` (cit. on p. 2).

[19] S. P. Martin, *A Supersymmetry primer*,
Adv. Ser. Direct. High Energy Phys. **18** (1998) 1, ed. by G. L. Kane, arXiv: `hep-ph/9709356` (cit. on p. 2).

[20] T. Abe, M. Fujiwara and J. Hisano,
Loop corrections to dark matter direct detection in a pseudoscalar mediator dark matter model,
JHEP **02** (2019) 028, arXiv: `1810.01039 [hep-ph]` (cit. on p. 2).

[21] M. Bauer, U. Haisch and F. Kahlhoefer,
Simplified dark matter models with two Higgs doublets: I. Pseudoscalar mediators,
JHEP **05** (2017) 138, arXiv: `1701.07427 [hep-ph]` (cit. on pp. 3, 4, 18, 21).

[22] T. Abe et al., *LHC Dark Matter Working Group: Next-generation spin-0 dark matter models*, Phys. Dark Univ. **27** (2020) 100351, arXiv: `1810.09420 [hep-ex]` (cit. on pp. 3–5, 8, 18, 22, 23).

[23] ATLAS Collaboration, *Constraints on mediator-based dark matter and scalar dark energy models using $\sqrt{s} = 13$ TeV pp collision data collected by the ATLAS detector*, JHEP **05** (2019) 142, arXiv: `1903.01400 [hep-ex]` (cit. on pp. 3, 5, 8, 18, 20–22).

[24] CMS Collaboration, *Search for dark matter produced in association with a Higgs boson decaying to a pair of bottom quarks in proton–proton collisions at $\sqrt{s} = 13$ TeV*, Eur. Phys. J. C **79** (2019) 280, arXiv: `1811.06562 [hep-ex]` (cit. on p. 3).

[25] CMS Collaboration, *Search for dark matter produced in association with a leptonically decaying Z boson in proton–proton collisions at $\sqrt{s} = 13$ TeV*, Eur. Phys. J. C **81** (2021) 13, arXiv: `2008.04735 [hep-ex]` (cit. on p. 3).

[26] ATLAS Collaboration, *Search for Dark Matter produced in association with a Standard Model Higgs boson decaying to b-quarks using the full Run 2 collision data with the ATLAS detector*, ATLAS-CONF-2021-006, 2021, URL: `https://cds.cern.ch/record/2759211`
(cit. on pp. 3, 7–9).

[27] ATLAS Collaboration, *Search for associated production of a Z boson with an invisibly decaying Higgs boson or dark matter candidates at $\sqrt{s} = 13$ TeV with the ATLAS detector*, ATLAS-CONF-2021-029, 2021, URL: `https://atlas.web.cern.ch/Atlas/GROUPS/PHYSICS/CONFNOTES/ATLAS-CONF-2021-029`
(cit. on pp. 3, 7, 8).

[28] ATLAS Collaboration, *Search for dark matter produced in association with a single top quark in $\sqrt{s} = 13$ TeV pp collisions with the ATLAS detector*, (2020), arXiv: `2011.09308 [hep-ex]`
(cit. on pp. 3, 8, 10, 18, 19).

[29] ATLAS Collaboration, *Search for charged Higgs bosons decaying into a top quark and a bottom quark at $\sqrt{s}$=13 TeV with the ATLAS detector*, (2021), arXiv: `2102.10076 [hep-ex]`
(cit. on pp. 3, 8, 10).

[30] J. F. Gunion and H. E. Haber,
The CP conserving two Higgs doublet model: The Approach to the decoupling limit,
Phys. Rev. D **67** (2003) 075019, arXiv: `hep-ph/0207010` (cit. on pp. 3, 4).

[31] P. Pani and G. Polesello, *Dark matter production in association with a single top-quark at the LHC in a two-Higgs-doublet model with a pseudoscalar mediator*, Phys. Dark Univ. **21** (2018) 8, arXiv: `1712.03874 [hep-ph]` (cit. on pp. 5, 18, 19).

[32] ATLAS Collaboration, *ATLAS data quality operations and performance for 2015–2018 data-taking*, JINST **15** (2020) P04003, arXiv: `1911.04632 [physics.ins-det]` (cit. on p. 5).

[33] C. Degrande et al., *UFO - The Universal FeynRules Output*,
Comput. Phys. Commun. **183** (2012) 1201, arXiv: `1108.2040 [hep-ph]` (cit. on p. 5).

[34] J. Alwall et al., *The automated computation of tree-level and next-to-leading order differential cross sections, and their matching to parton shower simulations*, JHEP **07** (2014) 079, arXiv: `1405.0301 [hep-ph]` (cit. on p. 5).

[35] T. Sjöstrand et al., *An introduction to PYTHIA 8.2*, Comput. Phys. Commun. **191** (2015) 159, arXiv: `1410.3012 [hep-ph]` (cit. on p. 5).

[36] ATLAS Collaboration, *ATLAS Pythia 8 tunes to* 7 *TeV data*, ATL-PHYS-PUB-2014-021, 2014, URL: `https://cds.cern.ch/record/1966419` (cit. on p. 5).

[37] R. D. Ball et al., *Parton distributions for the LHC Run II*, JHEP **04** (2015) 040, arXiv: `1410.8849 [hep-ph]` (cit. on p. 5).

[38] *[2HDM+a] future generation settings*, URL: `https://groups.cern.ch/group/lhc-dmwg-contributors/Lists/Archive/Flat.aspx?RootFolder=%2Fgroup%2Flhc%2Ddmwg%2Dcontributors%2FLists%2FArchive%2F%5B2HDM%2Ba%5D%20future%20generation%20settings&FolderCTID=0x012002005558754F555BC94A8DE741034E6A95C1` (cit. on p. 6).

[39] ATLAS Collaboration, *Summary of ATLAS Pythia 8 tunes*, ATL-PHYS-PUB-2012-003, 2012, URL: `https://cds.cern.ch/record/1474107` (cit. on p. 6).

[40] A. D. Martin, W. J. Stirling, R. S. Thorne and G. Watt, *Parton distributions for the LHC*, Eur. Phys. J. C **63** (2009) 189, arXiv: `0901.0002 [hep-ph]` (cit. on p. 6).

[41] ATLAS Collaboration, *The ATLAS Simulation Infrastructure*, Eur. Phys. J. C **70** (2010) 823, arXiv: `1005.4568 [physics.ins-det]` (cit. on p. 6).

[42] S. Agostinelli and others., *Geant4—a simulation toolkit*, Nuclear Instruments and Methods in Physics Research Section A: Accelerators, Spectrometers, Detectors and Associated Equipment **506** (2003) 250, ISSN: 0168-9002, URL: `https://www.sciencedirect.com/science/article/pii/S0168900203013688` (cit. on p. 6).

[43] ATLAS Collaboration, *The simulation principle and performance of the ATLAS fast calorimeter simulation FastCaloSim*, ATL-PHYS-PUB-2010-013, 2010, URL: `https://cds.cern.ch/record/1300517` (cit. on p. 6).

[44] O. Mattelaer, *On the maximal use of Monte Carlo samples: re-weighting events at NLO accuracy*, Eur. Phys. J. C **76** (2016) 674, arXiv: `1607.00763 [hep-ph]` (cit. on p. 7).

[45] ATLAS Collaboration, *Search for dark matter in events with missing transverse momentum and a Higgs boson decaying into two photons in proton–proton collisions at* $\sqrt{s} = 13$ *TeV with the ATLAS detector*, (2021), arXiv: `2104.13240 [hep-ex]` (cit. on pp. 7, 9).

[46] ATLAS Collaboration, *Combination of searches for invisible Higgs boson decays with the ATLAS experiment*, ATLAS-CONF-2020-052, 2020, URL: `https://cds.cern.ch/record/2743055` (cit. on pp. 8, 11, 12).

[47] ATLAS Collaboration, *Search for invisible Higgs boson decays with vector boson fusion signatures with the ATLAS detector using an integrated luminosity of* $139\,fb^{-1}$, ATLAS-CONF-2020-008, 2020, URL: `https://cds.cern.ch/record/2715447` (cit. on p. 11).

[48] ATLAS Collaboration, *Search for a scalar partner of the top quark in the all-hadronic* $t\bar{t}$ *plus missing transverse momentum final state at* $\sqrt{s} = 13$ *TeV with the ATLAS detector*, Eur. Phys. J. C **80** (2020) 737, arXiv: `2004.14060 [hep-ex]` (cit. on p. 11).

[49] ATLAS Collaboration, *Search for new phenomena in events with two opposite-charge leptons, jets and missing transverse momentum in pp collisions at* $\sqrt{s} = 13$ *TeV with the ATLAS detector*, ATLAS-CONF-2020-046, 2020, URL: https://cds.cern.ch/record/2728056 (cit. on p. 11).

[50] ATLAS Collaboration, *Constraints on new phenomena via Higgs boson couplings and invisible decays with the ATLAS detector*, JHEP **11** (2015) 206, arXiv: 1509.00672 [hep-ex] (cit. on p. 11).

[51] ATLAS Collaboration, *Procedure for the LHC Higgs boson search combination in summer 2011*, ATL-PHYS-PUB-2011-011, 2011, URL: https://cds.cern.ch/record/1375842 (cit. on p. 11).

[52] K. Cranmer, G. Lewis, L. Moneta, A. Shibata and W. Verkerke, *HistFactory: A tool for creating statistical models for use with RooFit and RooStats*, tech. rep., New York U., 2012, URL: https://cds.cern.ch/record/1456844 (cit. on p. 11).

[53] A. L. Read, *Presentation of search results: the* CL_S *technique*, J. Phys. G **28** (2002) 2693 (cit. on p. 12).

[54] G. Cowan, K. Cranmer, E. Gross and O. Vitells, *Asymptotic formulae for likelihood-based tests of new physics*, Eur. Phys. J. C **71** (2011) 1554, arXiv: 1007.1727 [physics.data-an] (cit. on p. 12), Erratum: Eur. Phys. J. C **73** (2013) 2501.

[55] L. Moneta et al., *The RooStats Project*, (2011), arXiv: 1009.1003 [physics.data-an] (cit. on p. 12).

[56] W. Verkerke and D. Kirkby, *The RooFit toolkit for data modeling*, 2003, arXiv: physics/0306116 [physics.data-an] (cit. on p. 12).

[57] ATLAS Collaboration, *Combined measurements of Higgs boson production and decay using up to* $80\,fb^{-1}$ *of proton–proton collision data at* $\sqrt{s} = 13$ *TeV collected with the ATLAS experiment*, Phys. Rev. D **101** (2020) 012002, arXiv: 1909.02845 [hep-ex] (cit. on p. 12).

[58] R. Herbrich, *Learning Kernel Classifiers: Theory and Algorithms*, Cambridge, MA, USA: MIT Press, 2001, ISBN: 026208306X (cit. on p. 13).

[59] I. Steinwart and A. Christmann, *Support Vector Machines*, 1st, Springer Publishing Company, Incorporated, 2008, ISBN: 0387772413 (cit. on p. 13).

[60] U. Haisch and G. Polesello, *Searching for heavy Higgs bosons in the* $t\bar{t}Z$ *and* tbW *final states*, JHEP **09** (2018) 151, arXiv: 1807.07734 [hep-ph] (cit. on p. 18).

[61] ATLAS Collaboration, *Search for dark matter in events with a hadronically decaying vector boson and missing transverse momentum in pp collisions at* $\sqrt{s} = 13$ *TeV with the ATLAS detector*, JHEP **10** (2018) 180, arXiv: 1807.11471 [hep-ex] (cit. on p. 18).

[62] ATLAS Collaboration, *Search for dark matter produced in association with bottom or top quarks in* $\sqrt{s} = 13$ *TeV pp collisions with the ATLAS detector*, Eur. Phys. J. C **78** (2018) 18, arXiv: 1710.11412 [hep-ex] (cit. on pp. 20, 22).

[63] ATLAS Collaboration, *Search for top-squark pair production in final states with one lepton, jets, and missing transverse momentum using* $36\,fb^{-1}$ *of* $\sqrt{s} = 13$ *TeV pp collision data with the ATLAS detector*, JHEP **06** (2018) 108, arXiv: 1711.11520 [hep-ex] (cit. on p. 20).

[64] ATLAS Collaboration, *Search for new phenomena in a lepton plus high jet multiplicity final state with the ATLAS experiment using* $\sqrt{s} = 13$ *TeV proton–proton collision data*, JHEP **09** (2017) 088, arXiv: 1704.08493 [hep-ex] (cit. on p. 20).

[65] A. Djouadi, M. Drees and J.-L. Kneur,
Neutralino dark matter in mSUGRA: Reopening the light Higgs pole window,
Phys. Lett. B **624** (2005) 60, arXiv: `hep-ph/0504090 [hep-ph]` (cit. on pp. 22, 23).

[66] E. A. Bagnaschi et al., *Supersymmetric dark matter after LHC Run 1*, Eur. Phys. J. C **75** (2015) 500, arXiv: `1508.01173 [hep-ph]` (cit. on pp. 22, 23).